Modeling the whole atmosphere response to solar cycle changes in radiative and geomagnetic forcing

D. R. Marsh,[1] R. R. Garcia,[1] D. E. Kinnison,[1] B. A. Boville,[1] F. Sassi,[1] S. C. Solomon,[1] and K. Matthes[2,3]

[1] The NCAR Whole Atmosphere Community Climate Model, version 3 (WACCM3), is used to study the atmospheric response from the surface to the lower thermosphere to changes in solar and geomagnetic forcing over the 11-year solar cycle. WACCM3 is a general circulation model that incorporates interactive chemistry that solves for both neutral and ion species. Energy inputs include solar radiation and energetic particles, which vary significantly over the solar cycle. This paper presents a comparison of simulations for solar cycle maximum and solar cycle minimum conditions. Changes in composition and dynamical variables are clearly seen in the middle and upper atmosphere, and these in turn affect terms in the energy budget. Generally good agreement is found between the model response and that derived from satellite observations, although significant differences remain. A small but statistically significant response is predicted in tropospheric winds and temperatures which is consistent with signals observed in reanalysis data sets.

Citation: Marsh, D. R., R. R. Garcia, D. E. Kinnison, B. A. Boville, F. Sassi, S. C. Solomon, and K. Matthes (2007), Modeling the whole atmosphere response to solar cycle changes in radiative and geomagnetic forcing, *J. Geophys. Res.*, *112*, D23306, doi:10.1029/2006JD008306.

1. Introduction

[2] As the quality and time span of atmospheric measurements increases, there is growing evidence that changes in solar radiative forcing and energetic particle fluxes affect all regions of the atmosphere. Clear signals are found in the stratosphere, where a combination of satellite and ground-based observations dating from the 1980s have been used to show a good correlation between ultraviolet (UV) flux changes output over the 11-year sunspot cycle and ozone, geopotential height, and temperature (see, e.g., reviews by *van Loon and Labitzke* [2000] and *Hood* [2004]). Springtime Southern Hemisphere enhancements in stratospheric nitrogen dioxide (NO_2) are thought to be the result of particle precipitation at higher altitudes [*Siskind*, 2000; *Randall et al.*, 2001]. In the mesosphere, decadal variations are seen in temperature [*Remsberg and Deaver*, 2005], water vapor [*Chandra et al.*, 1997], and polar mesospheric clouds [*DeLand et al.*, 2003, 2006]. In the lower thermosphere a strong correlation is seen between nitric oxide (NO) concentrations and proxies for UV and geomagnetic activity [*Marsh et al.*, 2004]. Several observational studies show a significant response of the troposphere to the solar cycle. For example, *Haigh* [2003] and *Haigh et al.* [2005] extracted a statistically significant solar signal from National Centers for Environ-

mental Prediction/National Center for Atmospheric Research (NCEP/NCAR) reanalysis zonal mean temperatures and zonal winds using a multiple regression technique. Similar results were obtained by *Crooks and Gray* [2005] who analyzed the European Centre for Medium-Range Weather Forecasts 40-year reanalysis (ERA-40) data set. *Coughlin and Tung* [2004] used empirical mode decomposition of the NCEP/NCAR reanalysis data between 1958 and 2003. They found that the atmosphere below 10 hPa is warmer over most of the globe during solar maximum relative to solar minimum. Finally, *Thejll et al.* [2003] report a highly significant correlation over the period 1973 to 2000 between a smoothed geomagnetic index and both the North Atlantic Oscillation index and geopotential heights in the Northern Hemisphere winter stratosphere. However, it should be pointed out that the physical processes by which geomagnetic variability could propagate to the lower atmosphere have not been determined.

[3] Over the last decade, atmospheric models have increased in complexity to a point where many of the solar-terrestrial coupling processes can be investigated. Several studies have used general circulation models (GCMs) to investigate the response of the atmosphere to imposed solar cycle variations in irradiance, heating, and ozone [e.g., *Haigh*, 1999; *Shindell et al.*, 1999, 2003; *Matthes et al.*, 2003]. Recently, GCMs have begun to incorporate interactive chemistry and an upper atmosphere, where solar induced changes in radiatively active gases can feed back on the model dynamical fields [*Tourpali et al.*, 2003; *Egorova et al.*, 2004; *Rozanov et al.*, 2004; *Schmidt et al.*, 2006; *Garcia et al.*, 2007; *Austin et al.*, 2007]. The use of

[1]National Center for Atmospheric Research, Boulder, Colorado, USA.
[2]Institut für Meteorologie, Freie Universität Berlin, Berlin, Germany.
[3]Also at National Center for Atmospheric Research, Boulder, Colorado, USA.

these 3-D models to study the solar cycle effects in the atmosphere is a natural progression from earlier 2-D studies [e.g., *Garcia et al.*, 1984; *Haigh*, 1994]. One benefit of using 3-D models is the explicit representation of planetary waves, which are thought to provide a mechanism by which the solar cycle can modulate the stratospheric polar night jet and the Brewer-Dobson circulation [*Kodera and Kuroda*, 2002]. Model accuracy has also been improved following recent satellite measurements of solar spectral variability in the ultraviolet (UV) that have led to better specification of the solar flux. For example, the solar cycle variation in spectral flux has been characterized using extended observations made by instruments on the Upper Atmosphere Research Satellite (UARS) [*Woods et al.*, 2000; *Woods and Rottman*, 2002]. This is especially important for models that do incorporate an upper atmosphere, since radiation absorbed in that region can vary to a far greater extent than the total solar irradiance, which only varies by approximately 0.1% over the solar cycle [*Lean et al.*, 1997]. Lastly, 3-D models are now incorporating energetic electron effects on stratospheric composition [*Langematz et al.*, 2005; *Rozanov et al.*, 2005]. These studies claim the magnitude of particle effects could be as large as those produced from solar radiative flux changes.

[4] Taken together, analysis of observations and model simulations have led to a better understanding of how the atmosphere responds to variations in radiative and geomagnetic forcing, and also to an improved capability in separating natural from anthropogenic influences. This paper presents new simulations of the "whole atmosphere" response to variability in solar and geomagnetic forcing using a three-dimensional (3-D) GCM with fully interactive chemistry. The following section describes the model, with particular attention to the specification of solar and geomagnetic forcing. Section 3 presents a comparison of the model response to constant forcing under solar maximum and minimum conditions. This is followed by discussion and summary in section 4.

2. Model Description

[5] WACCM3 is a global circulation model extending from the surface to the thermosphere based on version 3 of the Community Atmosphere Model (CAM3) [*Collins et al.*, 2004], which is the atmospheric component of the Community Climate System Model. The model has 66 levels that are spaced approximately 1.1−1.75 km apart in the troposphere and stratosphere, increasing to 3.5 km apart in the mesosphere and thermosphere. The horizontal resolution is 4° longitude by 5° latitude. Here WACCM3 is run coupled with a fully interactive chemistry module that includes both neutral and ionized species. Advection of constituents and dynamical quantities is handled by the finite-volume dynamical core of CAM3 [*Lin*, 2004]. In addition, because the model extends into the upper atmosphere (the model top pressure/altitude level is 5.1×10^{-6} hPa/∼140 km), many physical processes not included in CAM3 are incorporated into WACCM3. These include heating from exothermic chemical reactions, non-LTE radiative transfer, constituent ionization, molecular diffusion, joule heating, ion drag, and a modified gravity wave parameterization. This section describes the details of the

model most relevant to solar variability studies. Further discussion of model parameterizations (e.g., parameterizations of gravity waves and heterogeneous chemical processes within polar stratospheric clouds) is given by *Garcia et al.* [2007] and *Kinnison et al.* [2007].

[6] Simulations using WACCM have been compared with those from a dozen other coupled chemistry-climate models (as well as to observations) in the work by *Eyring et al.* [2006]. That study showed that WACCM simulations were in reasonable agreement with observed long-term trends in stratospheric temperature. In addition, indicators of stratospheric circulation such as the methane distribution, mean age of air, and the vertical propagation of the annual cycle in equatorial water vapor agreed well with observations [*Garcia et al.*, 2007].

2.1. Specification of Solar Spectral Irradiance

[7] WACCM3 uses a combination of parameterizations to specify solar spectral irradiances over two wavelength regions. Both parameterizations take as input the 10.7 cm solar radio flux ($f10.7$) and its 81-d average ($f10.7a$). Daily values of $f10.7$ are obtained from NOAA's Space Environment Center (http://www.sec.noaa.gov). The first spectral region covers soft X-ray and extreme ultraviolet irradiances (wavelengths between 0.05 nm and 121 nm in 23 spectral intervals) and is calculated using the parameterization of *Solomon and Qian* [2005]. The irradiance of the jth spectral interval is:

$$F_j = F_j^0 * \left\{ 1 + R_j * \left(\frac{f10.7 + f10.7a}{2} - F_{\min} \right) \right\} \quad (1)$$

where $F_{\min} = 80$. F_j^0 and R_j are taken from *Solomon and Qian* [2005, Table A1].

[8] Fluxes for the second interval between Lyman-α (121.6 nm) and 350 nm are specified at 1 nm resolution using the model based on UARS SOLSTICE measurements from *Woods and Rottman* [2002]. The irradiance of the jth spectral interval is:

$$\begin{aligned} F_j = F_j^0 * \bigg\{ &1 + \left(R_j^{27} - 1 \right) * \frac{f10.7 - f10.7a}{f_{27d}} \\ &+ \left(R_j^{11y} - 1 \right) * \frac{f10.7a - f_{\min}}{f_{\max} - f_{\min}} \bigg\} \end{aligned} \quad (2)$$

where $f_{\min} = 71$, $f_{\max} = 212$, and $f_{27d} = 73$. F_j^0 is the solar minimum spectral irradiance, and R_j^{27} and R_j^{11y} are the solar rotation and solar cycle variation factors (T. Woods, personal communication, 2004). Figure 1 shows the combined spectrum and its variability over the solar cycle. As expected, fluxes are generally larger at solar maximum, and the variability increases as the wavelength decreases. At 250 nm variations are around a few percent, increasing to 60% at Lyman-α, and fluxes in the EUV can increase by a factor of 2 or more. Finally, within the soft X-ray part of the spectrum, the increase is approximately 1−2 orders of magnitude.

2.2. Chemistry Model

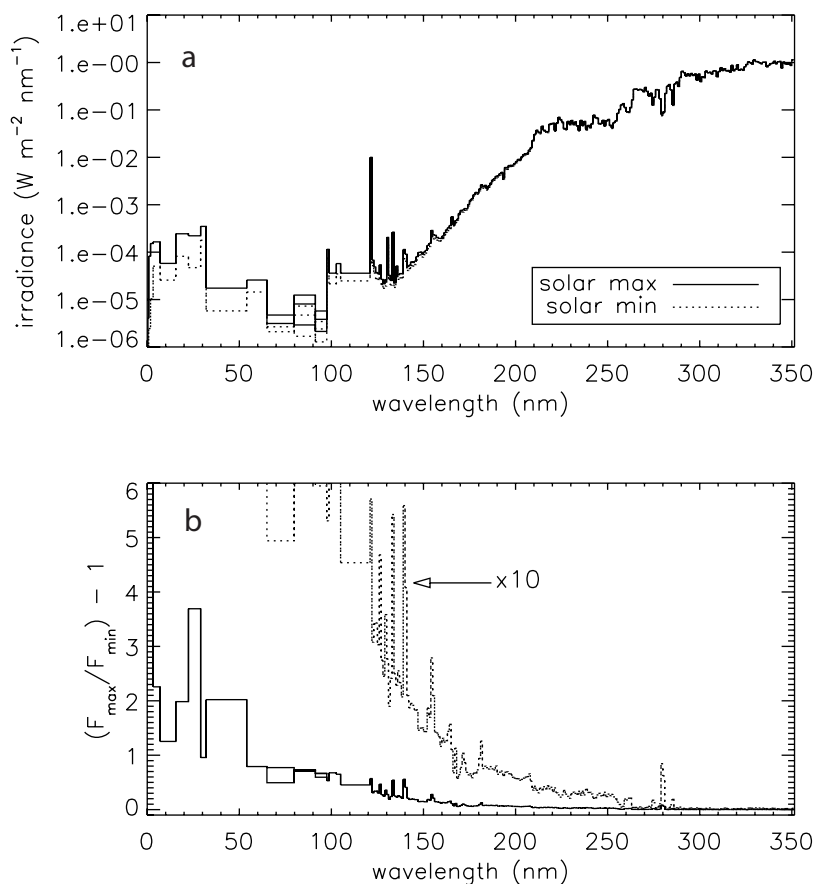[9] The chemistry module used in WACCM3 is version 3 of the Model for Ozone and Related Chemical Tracers

Figure 1. (a) Spectral irradiance (W m^{-2} nm^{-1}) between 0.05 nm and 350 nm used for solar maximum (solid line) and solar minimum conditions (dashed line). (b) Increase in spectral irradiance at solar maximum relative to solar minimum values.

(MOZART3). WACCM3 solves for 57 species and has 211 photochemical reactions. A description of the numerical solver and neutral gas phase and heterogeneous reactions is presented by *Kinnison et al.* [2007]. Reaction rate constants for the neutral chemistry are updated to the 2003 JPL recommendation [*Sander et al.*, 2003].

[10] The inclusion of a mesosphere and thermosphere necessitates the calculation of photolysis and photoionization frequencies over wavelengths much shorter than are usually considered in GCMs. CAM3, for example, only considers absorption of solar radiation longward of 200 nm. Photolysis and photoionization rates are calculated as a discrete sum over wavelength of the product of exoatmospheric spectral irradiance, absorption cross section, quantum yield, and a "radiative source function." For wavelengths greater than 200 nm a lookup table is used to obtain the radiative source function. The table is based on calculations from the Stratosphere, Troposphere, Ultraviolet (STUV) radiative transfer model (S. Madronich, personal communication, 2002), and is a function of altitude, column ozone, surface albedo, and zenith angle. STUV is based on the earlier model of *Madronich* [1989].

[11] At wavelengths less than 200 nm, scattering can be ignored and the radiative source function is essentially the transmittance, which is calculated inline. Depending on wavelength interval, this is calculated using a parameterization (e.g., *Koppers and Murtagh* [1996] within the

Schumann-Runge Bands) or using the Beer-Lambert law. Details of the cross sections and quantum yields for photolysis products are also presented by *Kinnison et al.* [2007]. Shortward of Lyman-α, photolysis and photoionization rates are calculated using the same parameterization of *Solomon and Qian* [2005] that provides irradiances (see section 2.1). This parameterization also provides ionization rates due to energetic secondary photoelectrons.

[12] WACCM3 includes a six-constituent ion chemistry model (O$^+$, O$_2^+$, N$^+$, N$_2^+$, NO$^+$, and electrons) that represents the E region ionosphere. The global mean ion and electron distributions simulated by WACCM3 for solar minimum conditions are shown in Figure 2, which clearly shows that the dominant ions in this region are NO$^+$ and O$_2^+$. Ion-neutral, recombination, and photoionization reactions included in WACCM3 are listed below and in Table 1:
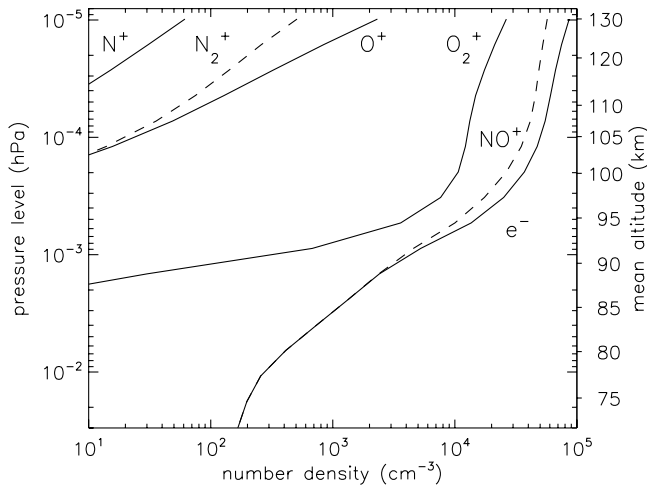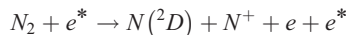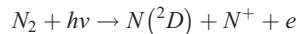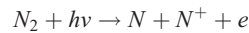
$$O + hv \rightarrow O^+ + e$$

$$O + e^* \rightarrow O^+ + e + e^*$$

$$N + hv \rightarrow N^+ + e$$

$$O_2 + hv \rightarrow O_2^+ + e$$
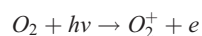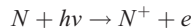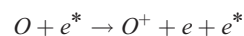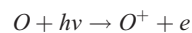
Figure 2. Global mean distribution of charged constituents during July solar minimum conditions.

$$O_2 + e^* \rightarrow O_2^+ + e + e^*$$

$$O_2 + h\nu \rightarrow O + O^+ + e$$

$$O_2 + e^* \rightarrow O + O^+ + e + e^*$$

$$N_2 + h\nu \rightarrow N_2^+ + e$$

$$N_2 + e^* \rightarrow N_2^+ + e + e^*$$

$$N_2 + h\nu \rightarrow N + N^+ + e$$

$$N_2 + e^* \rightarrow N + N^+ + e + e^*$$

$$N_2 + h\nu \rightarrow N\left(^2D\right) + N^+ + e$$

$$N_2 + e^* \rightarrow N\left(^2D\right) + N^+ + e + e^*$$
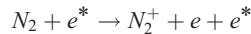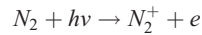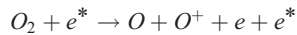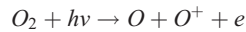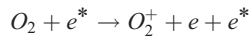
[13] The reaction rate constants for these reactions are taken from *Roble* [1995]. Because of the complexity of the D region ion chemistry, it is not possible to include it in the current chemical scheme. A model study by *Beig* [2000] predicted that the solar cycle could cause $20-30\%$ changes in total D region ion density between 70 and 88 km, but that study states that ion chemistry at these altitudes only affects the neutral composition significantly during solar particle events. Ionization sources include, not only the aforementioned absorption of extreme ultraviolet and soft X-ray photons, and photoelectron impact, but also energetic particle precipitation in the auroral regions. The latter is

obtained from a parameterization based on code from the NCAR TIME-GCM model [*Roble and Ridley*, 1994] that rapidly calculates ion-pair production rates, including production in the polar cusp and polar cap. The parameterization takes as input hemispheric power (HP), the estimated power in gigawatts deposited in the polar regions by energetic particles. Currently WACCM3 uses a parameterization of HP based on an empirical relationship of HP and the K_p planetary geomagnetic index by *Maeda et al.* [1989]:

$$HP(GW) = \max\left(3.0, -2.78 + 9.33 * K_p\right). \quad (3)$$

[14] K_p is also available from NOAA's Space Environment Center and covers the period from 1933 to the present, making it ideal for long-term retrospective simulations.

[15] Total ionization rates at 7.3×10^{-5} hPa ($\sim$110 km) during July for solar maximum conditions are shown in Figure 3a. The broad region of ionization centered in the tropics is a result of EUV ionization, and has a peak value of almost 10^4 cm^{-3} s^{-1} at 22°N. Ionization rates from particle precipitation can exceed this rate by 40% but are limited to the high latitudes, as can been seen by the two bands that are approximately aligned around the magnetic poles. The combined ionization rate when viewed as a global mean (Figure 3b) is relatively constant with altitude above 105 km, but decreases sharply below that height, and is reduced by two orders of magnitude at 90 km.

[16] An important aspect of including ionization processes (both in the aurora and by energetic photons and photoelectrons), is that it leads to a more accurate representation of thermospheric nitric oxide. Not only does nitric oxide play an important role in the energy balance of the lower thermosphere through emission at 5.3 μm, it might also be transported to the upper stratosphere, where it can affect ozone concentrations. Nitric oxide is produced through the reaction of molecular oxygen with N(^{2}D):

$$N\left(^2D\right) + O_2 \rightarrow NO + O\left(^1D\right) + 1.84eV \quad (4)$$
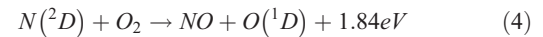
[17] N(^{2}D) is produced either via recombination of NO$^+$ (see Table 1) or directly by ionization of molecular nitrogen.

Table 1. Ion-Neutral and Recombination Reactions and Exothermicities

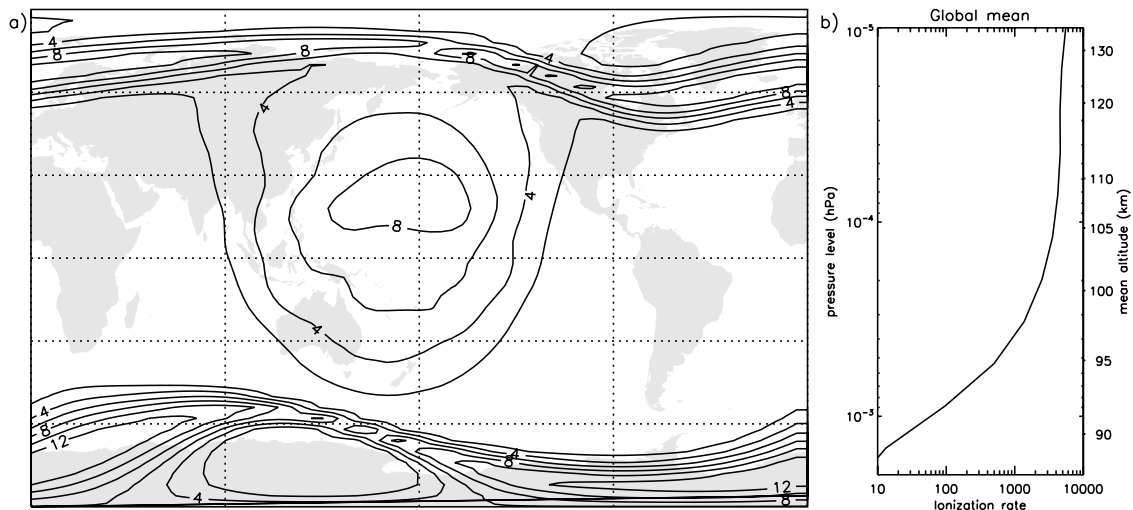|	ΔH, kJ mol^{-1}
$O^+ + O_2 \rightarrow O_2^+ + O$	150.11
$O^+ + N_2 \rightarrow NO^+ + N$	105.04
$N_2^+ + O \rightarrow NO^+ + N(^2D)$	67.53
$O_2^+ + N \rightarrow NO^+ + O$	406.16
$O_2^+ + NO \rightarrow NO^+ + O_2$	271.38
$N^+ + O_2 \rightarrow O_2^+ + N$	239.84
$N^+ + O_2 \rightarrow NO^+ + O$	646.28
$N^+ + O \rightarrow O^+ + N$	95.55
$N_2^+ + O_2 \rightarrow O_2^+ + N_2$	339.59
$O_2^+ + N_2 \rightarrow NO^+ + NO$	$-$
$N_2^+ + O \rightarrow O^+ + N_2$	$-$
$NO^+ + e \rightarrow 0.2N + 0.8N(^2D) + O$	82.389
$O_2^+ + e \rightarrow 1.15O + 0.85O(^1D)$	508.95
$N_2^+ + e \rightarrow 1.1N + 0.9N(^2D)$	354.83

Figure 3. (a) Global distribution of ionization rates at 7.3×10^{-5} hPa, 1 July, 0100 UT. Contour interval is 2×10^3 cm^{-3} s^{-1}. (b) Simultaneous global mean ionization rates (cm^{-3} s^{-1}) versus pressure.

The branching ratio between N(^{2}D) and ground-state atomic nitrogen (N(^{4}S)) for the photoionization process is critical in determining the effectiveness of NO production. If ground-state atomic nitrogen is produced, then it can react with NO to produce molecular nitrogen and effectively remove two members of the NO$_x$ family (NO$_x \equiv$ N + NO + NO$_2$). In WACCM3 60% of the atomic nitrogen produced is in the excited state, which implies absorption of EUV results in a net source of NO. In Figure 4b the zonal mean distribution of NO calculated by WACCM3 shows a broad maximum centered near 110 km, which is the result of EUV absorption. Also shown are maxima at high latitudes due to auroral ionization. WACCM3 reproduces many of the features of the Nitric Oxide Empirical Model (NOEM) distribution [*Marsh et al.*, 2004], which is based on data from the Student Nitric Oxide Explorer satellite [*Barth et al.*, 2003], and is shown in Figure 4a. In particular, larger NO in the winter hemisphere (a result of smaller photolytic loss), and a more localized NO maximum in the Northern Hemisphere (related to the smaller offset between the geographic and

magnetic poles, and thus smaller spread when viewed as a geographic zonal mean).

[18] Upper boundary conditions for most constituents are calculated using a zero flux condition. However, for some constituents that have large sources above the model upper boundary, constituent concentrations are constrained by empirical models. Atomic hydrogen, nitrogen, oxygen, and molecular oxygen are specified using the Naval Research Laboratory MSISE00 model [*Picone et al.*, 2002]. The upper boundary concentrations of nitric oxide are taken from NOEM. Finally, molecular hydrogen, carbon monoxide and carbon dioxide concentrations are taken from TIME-GCM simulations.

2.3. Energetics

[19] In the troposphere, stratosphere, and lower mesosphere (z < 65 km) WACCM3 retains the CAM3 shortwave heating (200 nm to 4.55 μm) which is calculated from the net shortwave spectral flux into each layer [*Collins et al.*, 2004]. The solar spectrum for the CAM3 heating calcula-
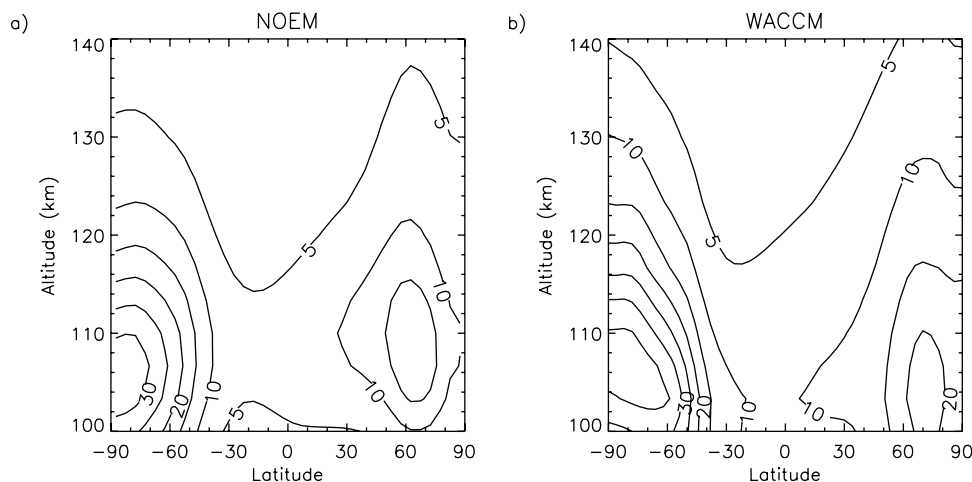

Figure 4. July zonal mean distributions of thermospheric nitric oxide concentrations (10^7 cm^{-3}) for solar minimum conditions: (a) Nitric Oxide Empirical Model and (b) WACCM3.
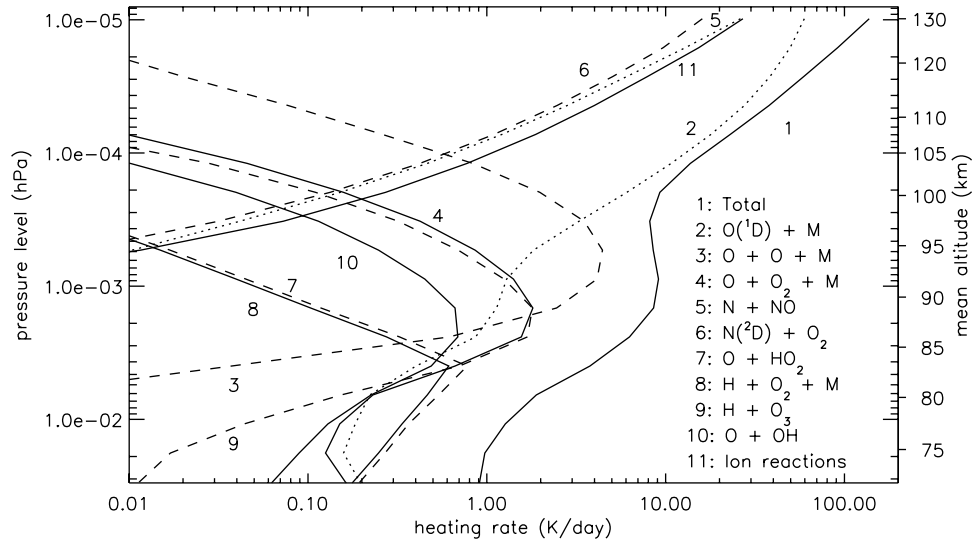
Figure 5. Global mean chemical heating rates (K/d) for 1 July during solar minimum conditions.

tion is divided into 19 intervals [*Collins*, 1998]. The fluxes in these intervals must be adjusted to match the irradiances calculated for the upper part of the model, and those used in the photolysis calculations. Shortward of 350 nm, this is achieved by applying a scaling (S_i) to the solar radiation in the ith CAM3 spectral interval using the spectrum from *Woods and Rottman* [2002]:

$$S_i = \frac{F_i(f10.7_a, f10.7)}{F_i(f10.7_{ref})}, \tag{5}$$

where F_i is the mean over the interval of fluxes given by (2). Between 200 nm and 350 nm there are 7 spectral bins that cover the Hartley band of ozone (bin centers at 222.5, 255, 270, 280, 290, 300, and 327.5 nm). Longward of 350 nm all bins are scaled with the following factor:

$$\overline{S} = \frac{R_{350}(f10.7)}{R_{350}(f10.7_{ref})}, \tag{6}$$

where $f10.7_{ref}$ is calculated such that,

$$\sum_{\lambda < 350nm} F_\lambda(f10.7_{ref}) + R_{350}(f10.7_{ref}) = TSI_{ref}. \tag{7}$$

[20] TSI_{ref} is the "standard" CAM3 total solar irradiance of 1367 W/m^2, and R_{350} is the total flux that lies above 350 nm. To calculate R_{350} the following formula is used:

$$R_{350} = a + b*f10.7a + c*(f10.7 - f10.7a) \tag{8}$$

where, a = 1307.81; b = 0.004996; and c = −0.009766. This formulation was designed to minimize the difference between the total solar irradiance (TSI) record between 1978 and 2004, and the integral spectral irradiance plus R_{350} calculated over the same period. The TSI data used to calculate R_{350} are version d30_60_0408 obtained from ftp://ftp.pmodwrc.ch/pub/data/irradiance/composite [*Froehlich*,

2000]. In effect, the scaling factor adjusts the flux uniformly in wavelength intervals longward of 350 nm (after the shorter fluxes have been adjusted by using the spectral model) in such a way as to fit the observed TSI variations.

[21] In the mesosphere and lower thermosphere (MLT), for altitudes >65 km, shortwave heating is the sum of the heating due to absorption of photons and subsequent exothermic chemical reactions that are initiated by photolysis. The majority of the energy deposited by an absorbed photon goes into breaking molecular bonds, rather than into translational energy of the absorbing molecule (heat). Chemical heating results when constituents react to form products of lower total chemical potential energy. This heating can take place months after the original photon absorption and thousands of kilometers away. Figure 5 shows global mean heating rates, in the range of altitude 75–130 km, from the most important chemical reactions in WACCM3. Heating rates range from 1 K/d near 75 km to 100–300 K/d near the top of the model domain. It is clear that quenching of O(^{1}D) is a large source of heating throughout the MLT. Above 100 km ion reactions and reactions involving atomic nitrogen are significant sources of heat, while below that level O$_x$($\equiv$O, O$_3$) and HO$_x$($\equiv$H, OH, HO$_2$) reactions are the dominant producers of chemical heating.

[22] Heating within the MLT from the absorption of radiation that is directly thermalized is calculated over the wavelength range of 0.05 nm to 350 nm. For wavelengths less than Lyman-α, it is assumed that 5% of the energy of each absorbed photon is directly thermalized [*Roble et al.*, 1987]:

$$Q_{EUV} = \epsilon(\rho c_p)^{-1} \sum_k n_k \sum_j J_k(\lambda_j) \frac{hc}{\lambda_j}, \tag{9}$$

where $\epsilon = 0.05$. Here ρ is mass density, c_p is the specific heat of dry air, n is the number density of the absorbing species, and J is the photolysis/photoionization rate. The total heating is the sum of k photolysis reactions and j wavelengths intervals. At these wavelengths absorption of a photon typically leads to photoionization, with the resulting
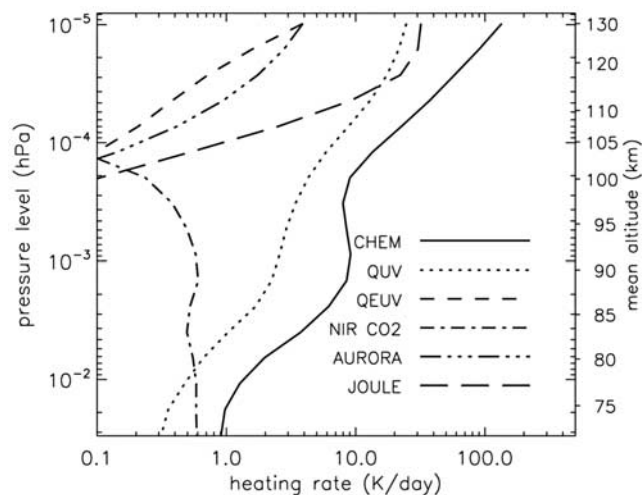
Figure 6. Heating rates (K/d) calculated in WACCM resulting from the absorption of solar radiation and energetic electrons. Heating rates are global means averaged for the month of July during solar minimum conditions. CHEM is chemical heating, QUV and QEUV are thermalized radiation (see text), NIR CO2 is heating by absorption of CO_2 in the near-infrared, AURORA is thermalized energy from particle precipitation, and JOULE is joule heating.

photoelectron having sufficient energy to ionize further molecules. J and ionization rates from photoelectrons are calculated on the basis of the parameterization of *Solomon and Qian* [2005]. As in the model of *Roble et al.* [1987] the majority of heating from EUV absorption comes from exothermic ion-neutral and neutral-neutral reactions, and the quenching of $O(^1D)$. In a similar manner, the heating rate within the aurora is calculated as the product of the total ionization rate, 35 eV per ion pair, and the same heating efficiency of 5%.

[23] Between Lyman-α and 350 nm the energy required to break molecular bonds is explicitly accounted for. The heating rate is thus defined as:

$$Q_{UV} = (\rho c_p)^{-1} \sum_k n_k \sum_j J_k(\lambda_j)\{\frac{hc}{\lambda_j} - BDE_k\}, \quad (10)$$

where *BDE* is the bond dissociation energy.

[24] In addition to these sources of heat, WACCM3 calculates heating by absorption in the near-infrared by CO_2 (between 1.05 to 4.3 μm), which has its largest contribution near 70 km and can exceed 1 K/d [*Fomichev et al.*, 2004]. Heating from this process is calculated using the parameterization of *Ogibalov and Fomichev* [2003]. Finally, the heating produced by collisions of electrons and neutrals (Joule heating) is also calculated using the predicted ion and electron concentrations, and the formulation of *Roble et al.* [1982]. Local heating rates from joule heating can be very large in the auroral regions, reaching over 10^3 K/d in the upper levels of the model.

[25] Airglow, radiation produced when excited atoms or molecules spontaneously emit, is accounted for in WACCM3 for emissions of $O_2(^1\Delta)$, $O_2(^1\Sigma)$, and vibration-

ally excited OH. Airglow from the excited molecular oxygen species are handled explicitly; radiative lifetimes for $O_2(^1\Delta)$ and $O_2(^1\Sigma)$ are 2.58×10^{-4} s^{-1} and 0.085 s^{-1} respectively [*Roble*, 1995]. However, modeling of the many possible vibrational transitions of OH is impractical in a global climate model such as WACCM3. Energy losses from the emission of vibrationally excited OH are therefore accounted for by applying an efficiency factor to the exothermicity of the reaction that produces vibrationally excited OH (i.e., the reaction of hydrogen and ozone). In other words, the reaction H + O_3 produces ground state OH only, but the chemical heating from the reaction has been reduced to take into consideration that some of the chemical potential energy is lost as airglow. This approach is the same one used by *Mlynczak and Solomon* [1993] and we use their recommended efficiency factor of 60%. Any energy lost through airglow is assumed to be lost to space, and so represents an energy pathway that does not generate heat.

[26] The global mean heating rates for the above processes are shown in Figure 6. Heating comes mostly from exothermic chemical reactions, including the quenching of $O(^1D)$, which is produced from photolysis of molecular oxygen at wavelengths below 176 nm, and photolysis of ozone at wavelengths below 310 nm. The second largest source of heating is from Joule heating, although in the auroral regions this heat source can exceed that from exothermic reactions. Other important heating terms include energy that is directly thermalized following absorption of radiation and energetic particles. In particular, Q_{UV} is the second most important heat source between 80 and 115 km.

[27] Longwave radiative transfer below ~60 km is calculated using the CAM3 parameterizations [*Collins et al.*, 2004], where local thermodynamic equilibrium (LTE) can be assumed. Above this altitude non-LTE conditions in the 15 μm band of CO_2 and the 9.6 μm band of ozone must be accounted for. WACCM3 uses the matrix parameterization of *Fomichev et al.* [1998], which was implemented in an earlier version of WACCM [*Sassi et al.*, 2002]. As mentioned previously, cooling from nitric oxide at 5.3 μm becomes an important radiative loss mechanism in the lower thermosphere. This cooling is calculated using the parameterization of *Kockarts* [1980].

3. Simulations

[28] Two simulations of 30 a each were run with fixed solar and geomagnetic forcing that are typical of conditions during solar maximum and minimum. Solar maximum conditions correspond to an $f10.7$ value of 210 and an A_p value of 27, while solar minimum is specified as $f10.7 = 77$ and $A_p = 12$. The A_p values selected correspond to HP values of 22 and 34 GW respectively. It should be noted that on a day-to-day basis the correlation between $f10.7$ and A_p is not particularly good (0.13 over the period 1948 and 2004), however, if 6 month averages are used, then the correlation is greater than 0.5. The correlation is largest if the A_p indices are lagged by about 16 months; that is, the maximum in geomagnetic activity in the last half century typically occurred early in the declining phase of the solar cycle. It therefore seems reasonable to examine the model differences between high solar/geomagnetic forcing and low solar/geomagnetic forcing. This type of scenario was used
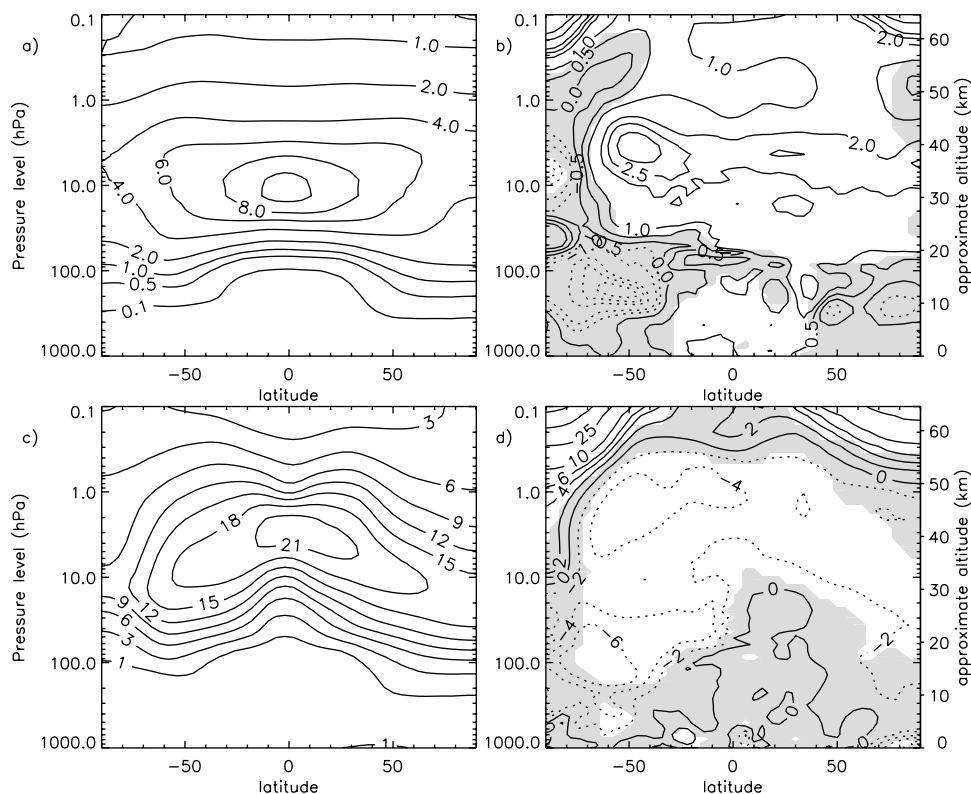
Figure 7. (a) Annual mean ozone volume mixing ratios (ppmv) for the solar minimum simulation. (b) Percent increases in ozone at solar maximum relative to solar minimum. (c and d) As in Figure s 7a and 7b for NOy. NOy mixing ratios are in ppbv.

previously in the two-dimensional model study of *Garcia et al.* [1984].

[29] Sea surface temperatures were the same in all simulations and are a climatological mean annual cycle based on a blend of Hadley Center and National Oceanic and Atmospheric Administration data sets [*Hurrell et al.*, 2006]. The concentrations of radiatively active gases at the lower boundary and the distribution of sulfate surface area density were held fixed at 1995 levels.

3.1. Solar Cycle Response of Constituents

[30] Of particular interest is the solar cycle response of stratospheric ozone, since it has been extensively measured and modeled. The annual mean ozone mixing ratio (parts per million by volume) distribution, and percentage change over the solar cycle are shown in Figures 7a and 7b. The solar response is statistically significant throughout a large portion of the stratosphere and lower mesosphere. Significance was determined using the Student's t-test, and unshaded regions in Figures 7a and 7b show a response significant at the 95% level. The response in this region exceeds 1% over the solar cycle, and near 4 hPa (~39 km) it is greater than 2% between 60°S and 90°N. The largest stratospheric solar cycle induced increase is 3.4%, and is seen at 50°S and 3 hPa. A local maximum (>3%) in the ozone response is also calculated for the same region of the stratosphere in the model study of *Rozanov et al.* [2004]. In comparison with the SOCOL model study of *Egorova et al.* [2004], the WACCM response is of comparable magnitude, but peaks at a slightly higher altitude. In addition, WACCM

does not show the a negative response in the region between 0.1 and 1 hPa that is predicted by the SOCOL model. The SOCOL model predicts a decrease of over 2% in tropical ozone around 0.2 hPa. This is interesting, since the *Egorova et al.* [2004] study uses the same GCM as a previous study by *Tourpali et al.* [2003], but includes a more accurate treatment of solar heating and photolysis in the middle atmosphere. However, the earlier study did not show a negative response of ozone in that region. In this respect, WACCM is in better agreement with the *Tourpali et al.* [2003] study, and it should be noted that the HAMMONIA model [*Schmidt et al.*, 2006] also does not show a negative response in ozone between 0.1 and 1 hPa.

[31] The magnitude of the ozone response is similar to that derived by *Soukharev and Hood* [2006] using Solar Backscattered Ultraviolet (SBUV-SBUV/2) satellite measurements. The SBUV data also shows the largest response in the Southern Hemisphere, centered between 60°S and 40°S. However, the height of the maximum response at the equator is about 9 km higher than WACCM3 in SBUV-SBUV/2 observations (which is centered near 1 hPa/~48 km), and the observed ~4% lower stratosphere response in also not reproduced. A recent analysis by *Randel and Wu* [2007] using Stratospheric Aerosol and Gas Experiment (SAGE I and II) ozone profile measurements between 1979 and 2005 yielded an ozone response closer to the height and magnitude of the one modeled in WACCM3. SAGE observations show only a 2.5% solar cycle response at the 3 hPa level near 30°S and at latitudes northward of
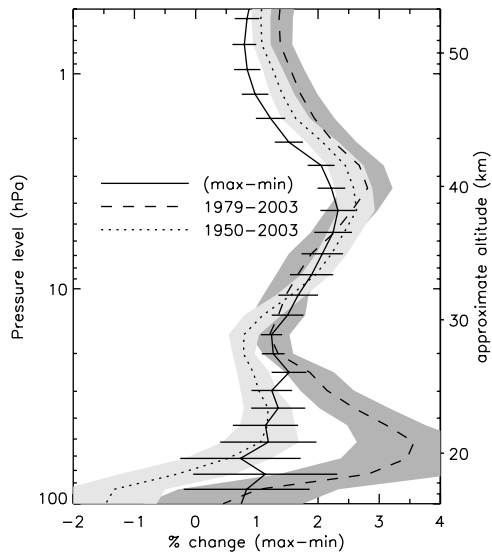
Figure 8. Percent increases in ozone at solar maximum relative to solar minimum averaged between 24°S to 24°N. Solid line, with 2σ error bars, is calculated from constant solar forcing "time slice" simulations. Lines with shaded regions are calculated using a multiple linear regression from the transient simulations of *Garcia et al.* [2007] for the time periods indicated. Shaded regions indicate 2σ errors in trend estimate.

[32] The vertical structure of the solar cycle response of WACCM3 annual mean ozone averaged over the latitude band 24°S to 24°N is shown in Figure 8. Additionally, the responses obtained by multiple-linear regression of WACCM3 transient simulations [*Garcia et al.*, 2007] are shown for selected time intervals. The regression analysis technique is identical to that used by *Garcia et al.* [2007] for total ozone, and the amplitudes shown are for 133 units of $f10.7$. All simulations place the maximum in upper stratospheric response around 40 km, and range between 2 and 3% over the solar cycle. Overall, the transient simulation response that most resembles the response in the fixed solar experiment is the one that is calculated from a regression over the 54 year period beginning 1950. This is probably due to a reduction of the influence of sporadic events (e.g., volcanic eruptions, ENSO) that could alias onto the solar cycle. The largest differences between the modeled responses are in the lower stratosphere. For example, the transient response between 1979 and 2003 is over 3.5% near 20 km, which is three times larger than the fixed solar and long-term transient response. Interestingly, this larger response is in good agreement with SBUV-SBUV/2 and Halogen Occultation Experiment (HALOE) observations [*Soukharev and Hood*, 2006]. The fact that this response is greatly reduced when a longer time series is considered indicates the current satellite record may not be long enough to isolate the solar response of the lower stratosphere.

[33] In Figure 7b there is a significant decrease in annual mean ozone between 30 and 40 km at high southern latitudes. Figure 9b shows that the decreases in ozone at the South Pole occur during winter and spring, and that the regions of depletion propagate downward with increasing time. In this region of the atmosphere, catalytic cycles involving the odd-nitrogen species NO and NO_2 are important sinks of ozone [*Brasseur and Solomon*, 2005]. If there is a solar cycle enhancement in these species, then there would be a negative response in ozone. Figures 7c and 7d show annual mean NOy (which is predominantly NO and NO_2 at these altitudes) and its change over the solar cycle. NOy at high latitudes is larger during solar maximum, with the largest changes seen in the Southern Hemisphere above 50 km. This increase is observed to a larger extent in the analysis of HALOE data by *Hood and Soukharev* [2006]

20°N. However, *Soukharev and Hood* [2006] also analyzed the SAGE data and report a response in excess of 4% near 25°S at the 3 hPa level. Both the SAGE and SBUV measurements indicate a slightly negative (not statistically significant) response in equatorial ozone between 10 and 30 hPa that is not produced in WACCM3. However, the modeling study of Lee and Smith indicates that the negative equatorial response in SAGE may be the result of aliasing of volcanic and quasi-biennial oscillation (QBO) effects onto the solar signal over the relatively short SAGE observational period. Since these steady state WACCM3 simulations do not include either a QBO or varying volcanic aerosols, it appears reasonable that WACCM3 does not reproduce the observed negative response.
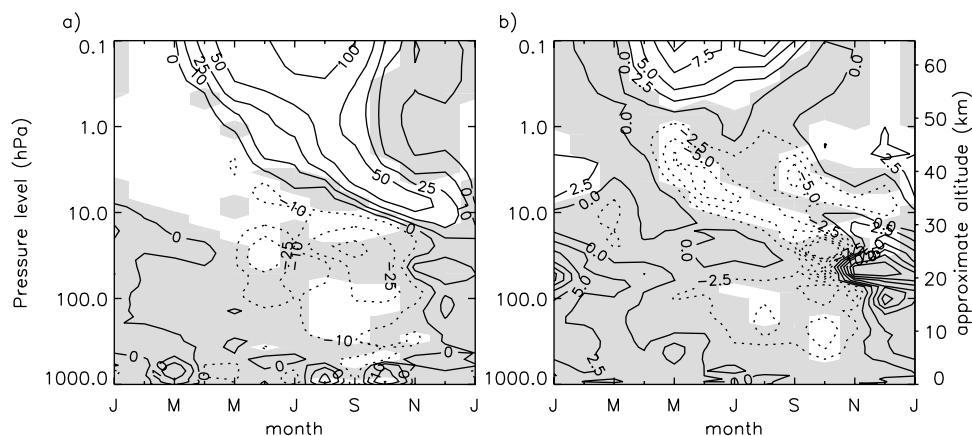

Figure 9. (a) Percent change in monthly mean NOy for solar maximum relative to solar minimum at 90°S. (b) As in Figure 9a but for ozone. Unshaded regions are significant at the 95% level.
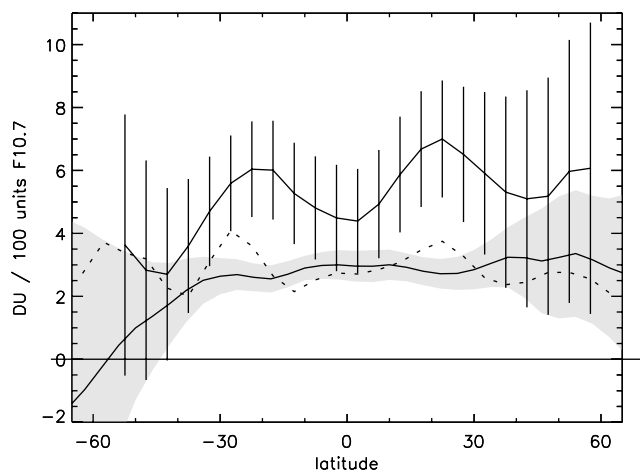
Figure 10. Zonally and annually averaged change in total ozone (DU/100 units of 10.7 cm flux) in WACCM3 (bottom line). Shaded region is the range of the 95% confidence interval. Satellite (top solid line) and ground-based (dashed line) estimates of total ozone change from *Randel and Wu* [2007].

using data from 1991 to 2003. They see increases of 70% in the southern lower mesosphere, but part of that increase is likely due to NO production during solar proton events that occurred near the maximum of solar cycle 23 [*Jackman et al.*, 2005]. These events are not included in the WACCM simulations shown here. The modeled increase is larger at higher altitudes, peaks during winter, and also appears to propagate downward with time (shown in Figure 9a). This is consistent with enhanced MLT NO (shown below) that is transported downward by the residual mean circulation under cover of polar night (in the daylit portion of the mesosphere photolytic losses destroy NO before it reaches the stratosphere). What is puzzling however, is that there is not a one-to-one correspondence between enhanced NOy and ozone depletion, and so there are likely a number of factors, such as dynamical variability, that contribute to winter and springtime middle stratosphere ozone loss. Nonetheless, NOy increases and ozone loss between September and November similar to those calculated in the model have been observed by the Polar Ozone and Aerosol Measurement (POAM II) instrument [*Randall et al.*, 1998]. In 1994, NO_2 increased by up to a factor of about 3 in late August following a period of enhanced geomagnetic activity, and subsequent to this NO_2 increase there was a $\sim$40% decrease in ozone. Just as in WACCM3, the observed ozone effects appear to be limited to altitudes above 22 km.

[34] Outside of polar night, at latitudes northward of approximately 70°S there is a slight ($\sim$3%) decrease in NOy throughout the stratosphere during solar maximum (Figure 7d). A similar response was observed in the HAMMONIA model [*Schmidt et al.*, 2006]. *Hood and Soukharev* [2006] also show a decrease in HALOE NOy, but it is confined to the latitudes equatorward of 30°, and is as large as −20%. Decreases in NOy are probably the result of an increase in NO photolysis rates, and the consequent reaction of the resulting atomic nitrogen with NO (a net loss of two NOy molecules). Figure 1 shows that fluxes between

180 nm and the predissociation limit of NO (about 191 nm) increase on average by 8%. The fact that the modeled decrease in NOy is less than the change in solar flux may indicate that increases in thermospheric NO due to larger EUV and auroral production is attenuating the flux that reaches the stratosphere. Consequently, thermospheric NO is shielding the stratospheric NO from the enhanced UV radiation (see *Minschwaner and Siskind* [1993] for a discussion on this topic).

[35] The modeled solar cycle induced change in zonal mean total ozone (in Dobson units per 100 units of 10.7 cm flux) averaged over the entire year as a function of latitude is shown in Figure 10. In the tropics the change is about 3 DU/100 units of 10.7 cm flux, which equates to 4 DU over the solar cycle. This is midway between the estimates made by the U.K. Meteorological Office Unified Model (5 DU) and the University of Tokyo Model (3 DU) reported by *Labitzke et al.* [2002]. The extratropical response in WACCM3 is similar to the University of Tokyo Model, in that it is relatively constant with latitude in the Northern Hemisphere and decreases toward the pole in the Southern Hemisphere. Just as in the other modeled responses, the uncertainty in the solar response becomes very large outside of the tropics. The response is also very similar to the response in WACCM3 transient simulations [*Garcia et al.*, 2007]. However, the WACCM3 response is substantially less than that calculated from satellite observations. Also shown in Figure 10 are *Randel and Wu* [2007] estimates of solar effects at latitudes less than 40° using Total Ozone Mapping Spectrometer (TOMS) and SBUV data. They show the effect to be between 3.6 and 7.0 DU/100 units of 10.7 cm flux, which is similar to the "merged satellite" response shown in WMO Assessment of Ozone Depletion [*World Meteorological Organization*, 2003]. While this is substantially higher than the WACCM3 response, it should be noted that the solar signal in ground-based total ozone observations (also shown in Figure 10) ranges approximately between 2 and 4 DU/100 units of 10.7 cm flux and so is in better agreement with the WACCM3 response. In general, it appears that the differences in the ozone solar cycle response between the model and observations are no larger than between differing sets of observations. The large uncertainty in the observational record is probably due to the relatively short period of observations (at most three solar cycles), and the presence of other perturbations that alias onto the solar signal (e.g., volcanic effects).

[36] Higher in the atmosphere, the magnitude of the ozone response is much larger, and in principle should be readily observed. The noon and midnight mesospheric ozone distributions for July are shown in Figures 11a and 11b. The ozone secondary maximum is clearly seen at both local times and is centered between $\sim$97–100 km in altitude. Midnight mixing ratios at the maximum are between 2 and 5 ppmv, which is about an order of magnitude larger than noon mixing ratios, caused by the absence of photolytic loss during nighttime. Secondary maximum daytime values in WACCM are about a third less than the observed values shown in studies of *Marsh et al.* [2002] and *Kaufmann et al.* [2003]. The reason for this model deficit is unclear, but a similar underprediction is observed in the HAMMONIA model. The solar cycle ozone response, shown in Figures 11c and 11d, varies with latitude, height and local
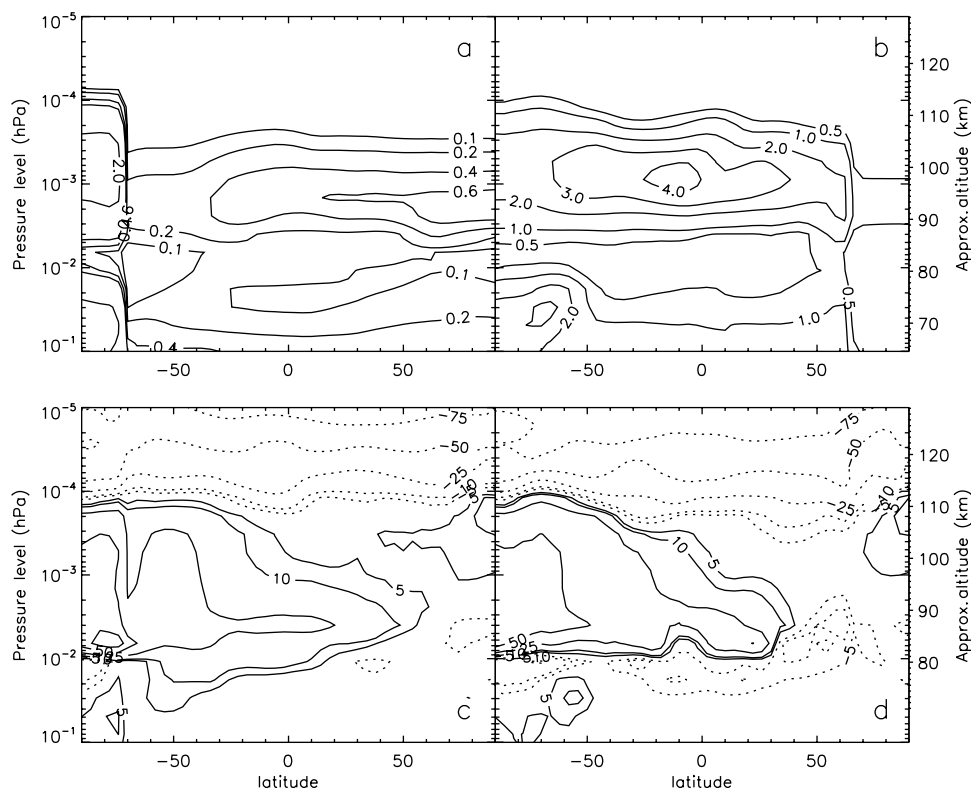
Figure 11. (a) Monthly mean ozone volume mixing ratios at noon local time in July for solar minimum conditions. (b) As Figure 11a but at midnight local time. (c and d) Percentage change for noon and midnight for solar maximum conditions relative to solar minimum.

time. During solar maximum, the ozone secondary maximum is larger than at solar minimum by as much as 50%, and the response is similar for noon and midnight. Above the secondary maximum the solar cycle response is negative, and also less ozone is seen at solar maximum during nighttime near 80 km. The variation in response can be understood by considering the ozone production and loss terms, assuming photochemical equilibrium. Ozone is produced via three-body recombination of atomic and molecular oxygen:

$$O + O_2 + M \rightarrow O_3 + M. \tag{11}$$
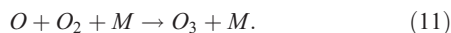
[37] Ozone concentrations are determined by a balance between production via (11) and losses through photolysis and the reaction with atomic hydrogen:

$$H + O_3 \rightarrow OH + O_2. \tag{12}$$
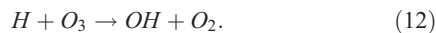
[38] Assuming photochemical equilibrium, and equating production to loss,

$$[O_3] = \frac{k[O][O_2][M]}{J_{O_3} + k'[H]}, \tag{13}$$

where [ ] denotes number density, k and k' are kinetic rate constants for (11) and (12), J_{O3} is the ozone photolysis rate (approximately 100 s^{-1}), and M is a third body (i.e., O, O$_2$, N$_2$). The secondary maximum is the result of sharply

increasing atomic oxygen concentrations (see Figure 12a) and the exponential dropoff of O$_2$ and N$_2$: ozone production is proportional to their product and so a layer is formed. Figure 12d shows that atomic oxygen also increases during solar maximum by 30–50%, and so production rates should increase accordingly. During the daytime, the loss mechanism is primarily via photolysis in the Hartley and Huggins bands (200–350 nm) which changes just a few percent over the solar cycle. Therefore solar induced changes in the daytime equilibrium value of ozone are very similar to the changes in atomic oxygen.

[39] The negative ozone response above the ozone secondary maximum, where admittedly there is very little ozone, is a consequence of changing temperatures. In the following section it is shown that temperatures in the lower thermosphere are higher at solar maximum. This affects ozone in two ways. First, warmer temperatures reduce k, the recombination rate constant, which has a T$^{-2.4}$ dependence [*Sander et al.*, 2003]. Secondly, on a constant pressure surface increased temperatures will decrease the total density, and therefore also reduce the recombination rate. The combination of these two effects substantially reduces ozone concentrations above 10^{-4} hPa (~110 km).

[40] Interestingly, at night there is also a reduction in ozone near 0.01 hPa (~80 km). This reduction is a result of increased losses by the reaction with hydrogen produced by Lyman-α photolysis of water vapor:
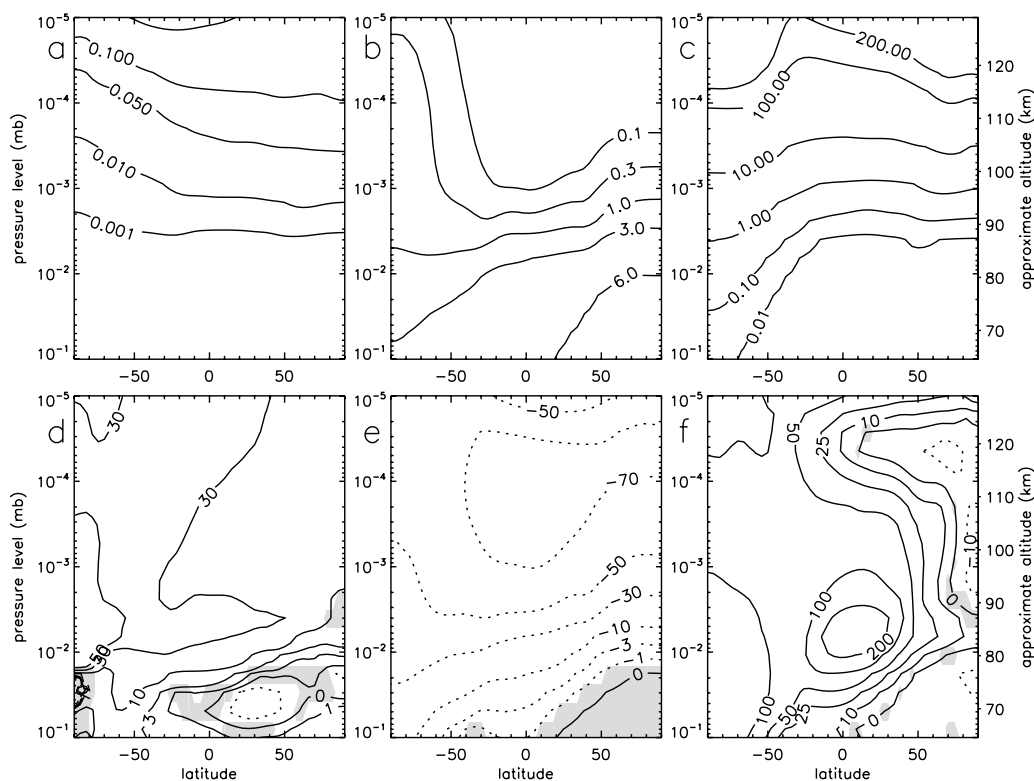
$$H_2O + h\nu(121.6nm) \rightarrow H + OH \tag{14}$$
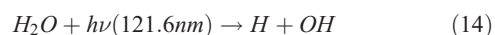
Figure 12. (a–c) July monthly mean volume mixing ratios of O, H_2O (ppmv), and NOx (ppmv). (d–f) Percentage change in O, H_2O, and NO_x for solar maximum conditions relative to solar minimum.

[41] The solar cycle effect on water vapor is large and clearly seen in Figure 12e and in observations made by HALOE [*Chandra et al.*, 1997; *Hervig and Siskind*, 2006]. At 0.007 hPa (~84 km) water vapor is between 4 and 43% less abundant at solar maximum than at solar minimum. The reduction is largest in the winter hemisphere because the residual circulation tends to bring air down from the thermosphere in winter and up from the lower mesosphere in summer. Lyman-α radiation is strongly attenuated below about 80 km, and so air originating below that height is not as affected by the solar cycle as air that originates in the thermosphere. The WACCM3 response is very similar to the response of the HAMMONIA model [*Schmidt et al.*, 2006].

[42] To date, the majority of mesospheric ozone studies have been based on data from the Solar Mesosphere Explorer (SME) near infrared spectrometer, between December 1981 and December 1986. Analysis of nearly 2 year of data from the same satellite by *Keating et al.* [1987] showed that between 65 and 75 km, there is a negative correlation between ozone density and solar ultraviolet flux. At 72 km they report that a 1% variation in Lyman-α flux leads to a −0.14% change in ozone. Above 75 km the response is positive, reaching 0.1 percent per percent at 80 km, which is thought to be due to an increase in odd-oxygen production by photolysis of molecular oxygen. The observed negative daytime response at 72 km is at odds with the simulated response, although the *Keating et al.* [1987] study was for short-term variability associated with solar rotation. In view of the new data sets from UARS and the Thermosphere

Ionosphere Mesosphere Energetics and Dynamics satellite [*Russell et al.*, 1999], the opportunity exists to revisit the mesospheric solar response.

[43] It should be noted that, while water vapor changes near the mesopause at the highest summer latitudes are relative small (1–10%) compared to those in the winter hemisphere, even these changes may influence the formation of polar mesospheric clouds (PMC). The study of *DeLand et al.* [2003] shows an anticorrelation between Lyman-α flux and PMC occurrence frequency, which is consistent with the reduced water vapor concentrations predicted by WACCM3 at solar maximum. To correctly model solar effects on PMC, WACCM3 will need to be modified to include a parameterization of PMC microphysics and run with higher vertical resolution. Such changes are planned for a future investigation of PMC.

[44] July mean mixing ratios for atomic oxygen and NO are shown in Figures 12a and 12c. Both constituents increase rapidly with height because of the presence of large thermospheric sources. The large horizontal gradient in NO is due to meridional transport, which will bring air rich in NO down in winter hemisphere. The gradient is not seen in atomic oxygen because atomic oxygen quickly combines with molecular oxygen in the MLT. As mentioned before atomic oxygen increases by 30–50% at solar maximum, which is the result of increased photolysis of molecular oxygen. NO is also higher during solar maximum, and this is due to combined increases in auroral particle precipitation and EUV fluxes. Higher fluxes at the shortest wavelengths (soft X rays) produce greater than
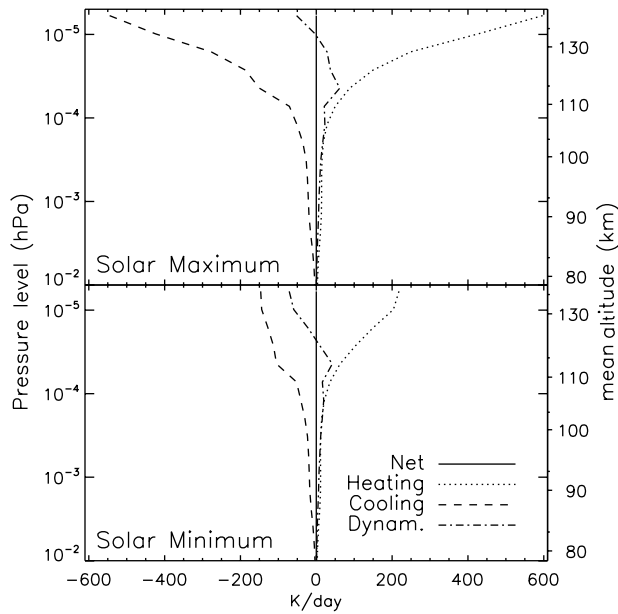
Figure 13. WACCM3 annual global mean MLT heating rates for (top) solar maximum and (bottom) solar minimum.

200% increase in NO mixing ratios at the mesopause in the tropics. Such increases cannot be transported to lower altitudes however, because the NO is quickly photolyzed. It is likely that aurorally produced NO in polar night is the source of the enhanced stratospheric NO seen in Figure 9.

3.2. Energetic and Dynamical Response

[45] Figure 13 shows global mean net heating, and cooling rates in the MLT averaged over the year for solar maximum and solar minimum. Net heating is very close

to zero and this is to be expected since the model integrations are long enough that annual mean temperatures do not have any significant trends under constant forcing and trace gas concentration boundary conditions. Zonally averaged heating rates (the sum of terms shown in Figure 6) show the largest solar signal in the topmost levels of the model. This is a consequence of the large changes in EUV and geomagnetic forcing, and the low densities in that region. Almost all of the heating terms shown in Figure 6 are considerably larger at solar maximum than solar minimum, the exception being CO_2 NIR heating, which is comparatively unchanged because of the low variability of radiation in the NIR. Consequently, the total heating increases by almost a factor of 3 at the 6.0×10^{-6} hPa level, is 38% larger at 7.3×10^{-5} hPa, and is 23% larger at 8.8×10^{-4} hPa. Changes in mean radiative cooling rates (also shown in Figure 13) at these same pressure levels are 270%, 36%, and 14% respectively. Radiative cooling, the sum of cooling by CO_2 and NO emissions, is dominated by CO_2 cooling during solar minimum. However, during solar maximum conditions, cooling from nitric oxide 5.3 μm emission increases dramatically (fourfold at 10^{-5} hPa), such that it is greater than CO_2 cooling down to the 2.0×10^{-5} hPa pressure level. NO 5.3 μm emission depends not only on the kinetic temperature, but also on the concentrations of atomic oxygen and nitric oxide [*Kockarts*, 1980]. Both of these constituents increase during solar maximum (as shown in Figure 12), and so the total 5.3 μm cooling rate is enhanced. A consequence of this is that cooling by diffusive transport of heat is reduced during solar maximum. This can seen Figure 13, where the height range over which dynamical cooling cools the thermosphere is reduced for solar maximum.

[46] Figure 14 shows the annual mean temperature for the whole model domain, and the solar cycle induced temper-
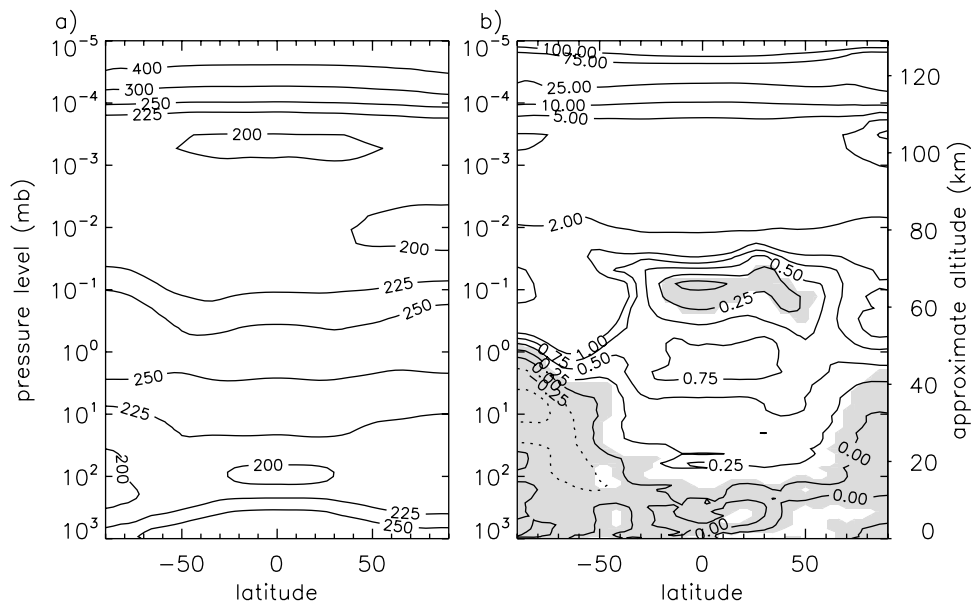

Figure 14. (a) Annual mean temperatures for the solar minimum simulation. (b) Temperature increases for the solar maximum simulation relative to temperatures in Figure 14a. Unshaded regions are significant at the 95% level.
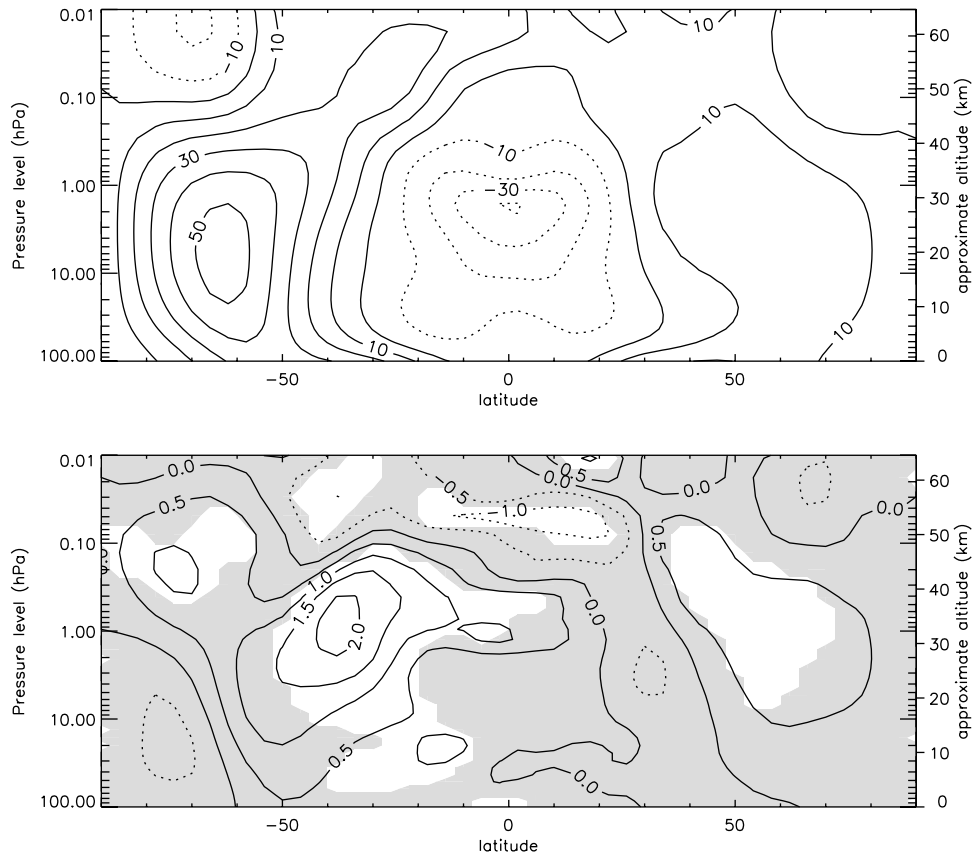
Figure 15. (top) Annual mean zonal mean zonal wind (m/s) and (bottom) its solar cycle–induced change (m/s). Unshaded regions are significant at the 95% level.

ature differences. Between ±50° latitude there is a statistically significant response throughout the stratosphere.

[47] The response peaks at the equator, with a maximum of 0.95 K at 1.6 hPa (∼45 km), and has a local minimum in the lower mesosphere near 0.1 hPa. The WACCM3 solar cycle temperature signal in the stratosphere is broadly similar to the signal in models included in the GCM-Reality Intercomparison Project for SPARC (GRIPS) study [*Matthes et al.*, 2003], and the more recent studies of *Rozanov et al.* [2004] and *Austin et al.* [2007]. Compared to observations, the distribution of the WACCM3 response is most similar to the response seen in Stratospheric Sounding Unit/Microwave Sounding Unit (SSU/MSU) satellite data [*Scaife et al.*, 2000; *Ramaswamy et al.*, 2001]. The peak in the satellite temperature data response centered near 40 km is slightly lower than in WACCM3, but the amplitude is very similar (in excess of 0.75 K over the solar cycle). However, the modeled temperature response is much smaller than the 2.5 ± 0.4 K response seen at 1 hPa in National Meteorological Center zonal mean temperatures [*McCormack and Hood*, 1996], and smaller than the ∼1.1 K for rocketsonde measured temperatures averaged vertically between 28 and 56 km [*Dunkerton et al.*, 1998]. The WACCM3 response is also smaller than the solar cycle signal calculated using linear regression from ERA-40 reanalysis data by *Crooks and Gray* [2005]. They saw a peak response of over 1.75 K near the equator. However, the height of the maximum response (2.5 hPa or 43 km) agrees

well with WACCM3. Considering the large variation in the responses calculated from observed temperatures, it is difficult to accurately assess the ability of WACCM3 to correctly simulate the stratospheric temperature response.

[48] The modeled annual mean zonal wind and its solar response are shown in Figure 15. The response is consistent with the temperature response: the relatively steep gradient in temperature around 40°S in the middle/upper stratosphere gives rise, through thermal wind balance, to a 2 m/s increase (more westerly) zonal winds. The response is weaker, but still significant in the opposite hemisphere. In general, the zonal wind response is less than is seen in ERA-40 winds [*Crooks and Gray*, 2005], but this is to be expected since the amplitude of the temperature response was also weaker.

[49] Since ozone is the dominant absorber of radiation in the stratosphere, radiative heating should change with changes in ozone. Hence an increase in ozone should lead to a increase in temperature. This is in addition to an increase in heating from larger UV fluxes. The sensitivity of ozone to temperature change has been investigated by *Froidevaux et al.* [1989]. They point out that negative temperature dependence of reaction (11) implies increased temperatures lead to decreased ozone concentrations, just as appears to be the case in the thermosphere. Thus a negative feedback mechanism exists that damps the response of ozone to changes in solar flux. Modeled stratospheric annual mean temperatures have a maximum increase at the equator (Figure 14), and this may be why the annual
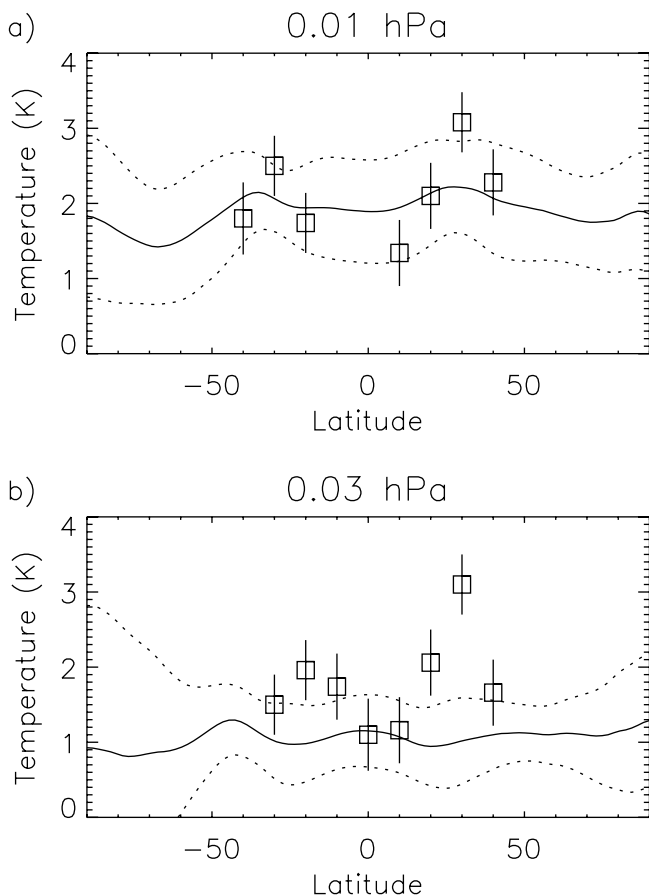
Figure 16. Comparison of solar maximum minus minimum annual mean temperature differences for WACCM3 (solid line) and HALOE (squares): (a) 0.01 hPa and (b) 0.03 hPa. Vertical and dotted lines are the 2-sigma uncertainties of the HALOE and WACCM3 responses.

mean ozone response peaks at midlatitudes. The sensitivity of ozone mixing ratio (f) on a constant pressure surface to temperature (T) can be approximated by the following formula used by *Froidevaux et al.* [1989]:

$$f = B \exp (\Theta/T), \tag{15}$$

where Θ and B are constants derived from observations made by the Limb Infrared Monitor of the Stratosphere. Therefore the change in ozone mixing ratio from ΔT change in temperature over the solar cycle is:

$$\frac{f_{min}}{f_{max}} = \exp \left(\frac{\Theta \Delta T}{T_{min}(T_{min} + \Delta T)} \right), \tag{16}$$

where at 3 hPa Θ was found to be 701 ± 83 K. Using WACCM3 temperatures from Figure 14, the calculated change in ozone due to solar induced changes in temperature at the equator is −0.8%. At 50°S, the change is only −0.26%, whereas at 50°N it is −0.67%. Therefore about half of the decrease in ozone response at the equator seen in Figure 7 can be attributed to an ozone temperature feedback. Such a response would only occur in a model

with interactive chemistry. Interestingly, the ozone response structure produced in WACCM3 is different from the equatorial maximum response produced in the 2-D model of *Lee and Smith* [2003], which does include interactive chemistry. In that model, a dipole structure is only produced when forcing by the QBO or volcanic eruptions is included.

[50] Poleward of 50° latitude the WACCM3 temperature solar signal is not significant below the 1 hPa level, because of the high level of variability in the polar stratosphere. The statistically significant modeled increase at latitudes poleward of 50°S above 1 hPa is also seen in the *Scaife et al.* [2000] SSU/MSU analysis. Above the local minimum in the solar cycle temperature response in the lower mesosphere, the response grows with height until, near the top of the model domain, it is greater than 100 K. A comparison of WACCM3 temperature differences in the mesosphere to those determined from the HALOE measurements is shown in Figure 16. The HALOE response is taken from *Remsberg and Deaver* [2005], who analyzed HALOE data from 1991 to 2004 using multiple linear regression. They found the amplitude of an 11-year solar cycle term to be 0.5 to 1.7 K (1 to 3.4 K peak-to-peak) in the middle mesosphere. The solar cycle response of WACCM3 is around 2 K in the tropics at the 0.01 hPa level, and is in good agreement with the HALOE measured response. However, WACCM3 shows a decrease in the response in the tropical lower mesosphere which is not evident in the observations. *Remsberg and Deaver* [2005] state that, between 0.05 hPa and 0.5 hPa, at latitudes less then 40°, the HALOE response is "weak and insignificant," and this also is the case for WACCM3 simulated response.

[51] *Hervig and Siskind* [2006] also analyzed solar signals in HALOE temperature, but for latitude bands centered at ±67.5°. Figure 17 shows the altitude distribution of the solar response at ±66° in WACCM (compare with *Hervig and Siskind*, [2006, Figure 6a]). The WACCM response is
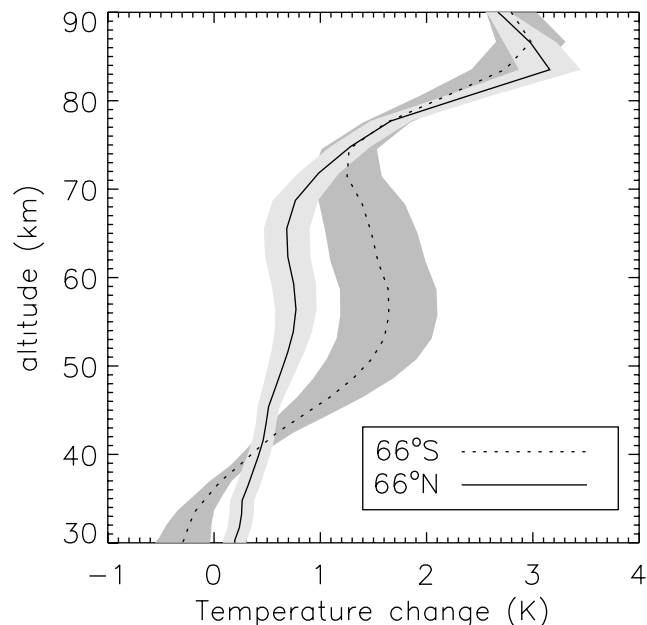

Figure 17. WACCM solar maximum minus minimum annual mean temperature differences at ±66° latitude. Shaded regions indicate 1-sigma uncertainties.
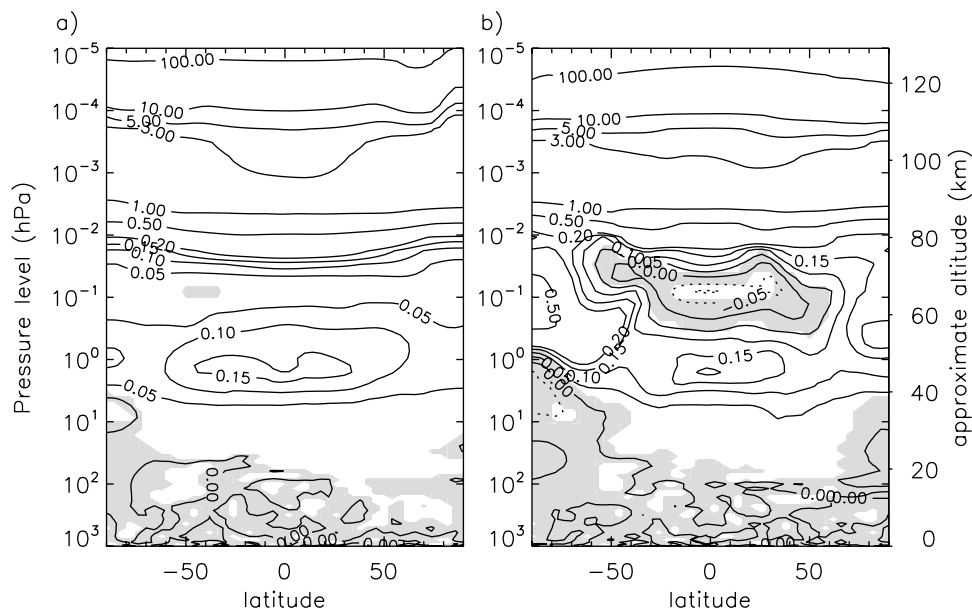
Figure 18.   Changes in (a) heating and (b) cooling rates in K/d for solar maximum conditions relative to solar minimum. Changes shown are annual mean zonally values. Unshaded regions are significant at the 95% level.

in good agreement with the calculated response from HALOE, and shows the same interhemispheric differences around 55 km: the Southern Hemisphere response is more than twice the response of the Northern Hemisphere. The response at 80 km is less than observed, but falls within calculated uncertainties. The temperature change in the high-latitude Northern Hemisphere at the mesopause (an important factor in the formation of PMC) during July (not shown) is approximately +1.7 ± 1 K. This is very similar to the +1.5 K seen in the HAMMONIA model [*Schmidt et al.*, 2006].

[52]   Figure 18 shows the solar cycle induced changes in annually averaged zonal mean heating and cooling rates. Since the model is in thermal equilibrium, differences between changes in heating and cooling rates must be balanced by dynamical processes. For example, as mentioned previously, differences in changes in the thermosphere are balanced by changes in thermal diffusion. In the equatorial stratopause region heating rates increases by up to 0.17 K/d during solar maximum. This increase is slightly less than 2% of the total heating rate, and is comparable to the change in solar flux near the center of the Hartley bands of ozone at 255 nm. The change in heating predicted by WACCM is less than that predicted in the GRIPS study of *Matthes et al.* [2003]: the MRI and FUB models show 0.21 K/d. This is most likely due to differences in the ozone responses in the models. The models in the GRIPS study used prescribed ozone changes from models that do not include fully inter-active chemistry. The prescribed ozone changes near the stratopause exceeded 3%, which is considerably larger then the 2−2.5% increase predicted by WACCM.

[53]   Since the primary heat source at the stratopause is from absorption of radiation by ozone, it is expected that these changes be approximately the same. The cooling response also peaks at the equator but is more confined in

latitude, which indicates dynamical transport must play a role cooling the midlatitudes.

[54]   At 1 hPa the global mean increase in heating and cooling (ΔQ) is ∼0.15 K/d, and the global mean temperature increase at that level (ΔT) (calculated from data shown Figure 14) is +0.74 K. The radiative lifetime, $\tau_{rad} = (\Delta Q/\Delta T)^{-1}$, is consequently around 5 d, which is in reasonable agreement with the value determined by *Mlynczak et al.* [1999] using satellite data.

[55]   Using a multiple regression technique *Haigh* [2003] found a significant solar cycle response in NCEP/NCAR tropospheric reanalysis zonal mean temperatures centered around ±40° latitude of approximately +0.5 K. The response was relatively constant with altitude, appearing as vertical bands of enhanced temperatures at midlatitudes, and little response at the equator. The latitude banding implies solar changes in temperature are more than simply a direct response to changes in radiative heating, which would be distributed more homogeneously in latitude. The same analysis of NCEP/NCAR zonal mean zonal winds [*Haigh et al.*, 2005] also shows a response that extends in vertical bands throughout the troposphere. The structure of the wind response is consistent with a weakening and poleward shift of the subtropical jets. The analysis of ERA-40 zonal winds and temperatures showed very similar responses [*Crooks and Gray*, 2005].

[56]   For comparison we show the annual mean of the WACCM3 zonal mean zonal wind in the troposphere in Figure 19 along with its change between solar maximum and minimum. There appears to be a significant, but small, response in the wind at midlatitudes, which is similar to the response found by *Haigh et al.* [2005] in NCEP/NCAR reanalysis data, i.e., a pattern consistent with a weakening and/or poleward shift of the subtropical jets. As in the observed response, the change appears as vertical bands. The annual mean temperature response (Figure 19c) is also
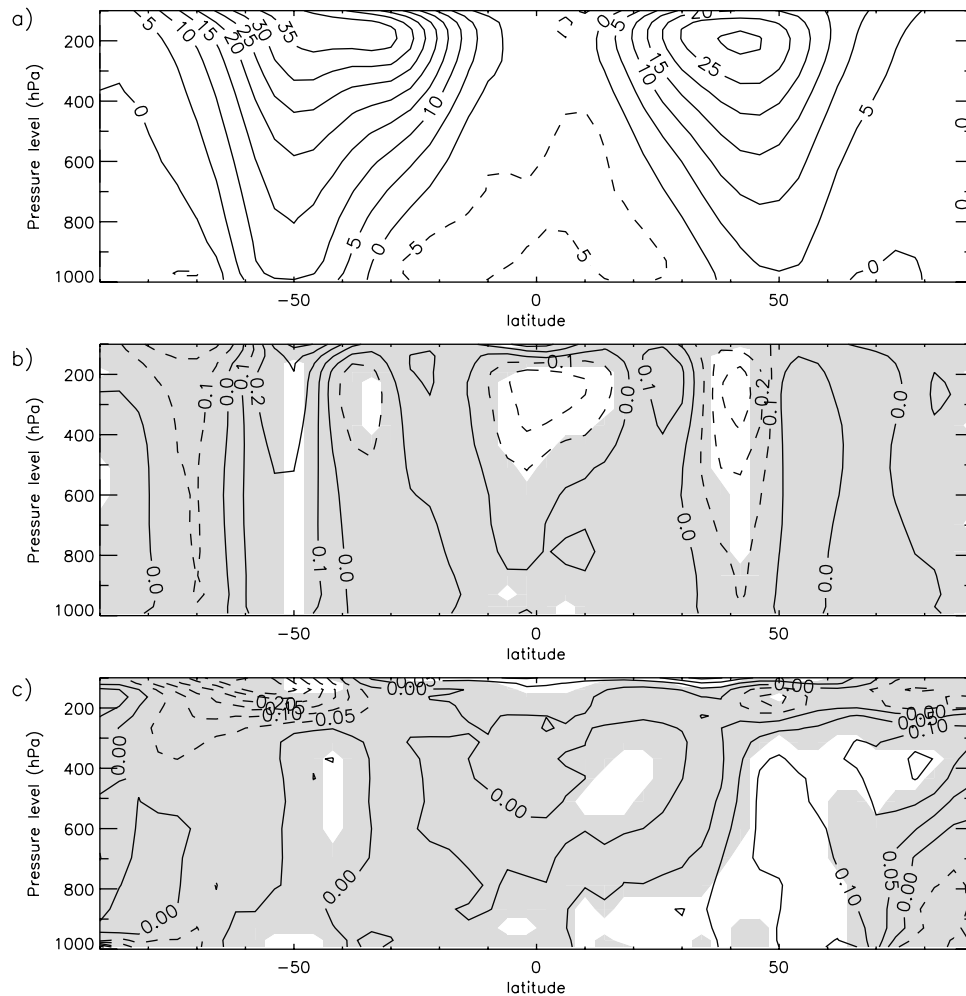
Figure 19. (a) Tropospheric annually and zonally averaged zonal winds (m/s) for solar minimum conditions. (b and c) Solar cycle changes (maximum-minimum) in annually and zonally averaged zonal winds (m/s) and zonal mean temperatures (K). Unshaded regions are significant at the 95% level.

significant at midlatitudes, but the amplitude of the response is between 1/2 and 1/5 of the observed responses reported by *Haigh et al.* [2005] and *Crooks and Gray* [2005]. The reduction in the response compared to observations may not be too surprising since both simulations used the same fixed sea surface temperatures (SSTs). *Rind et al.* [2005] showed that the response of the troposphere to changes in total solar irradiance was significantly reduced in a model run with prescribed SSTs when compared to a model run with an interactive ocean. A future study will look at the troposphere response in a version of WACCM3 that uses an interactive ocean model.

4. Summary and Discussion

[57] A GCM with coupled ion and neutral chemistry has been used to model the response of the whole atmosphere (surface to ~130 km) to variations in radiative and geomagnetic forcing typically seen over the 11-year solar sunspot cycle. This is the first time a GCM that extends to the surface includes a parameterization of auroral processes. The key findings are:

[58] 1. The largest atmospheric changes within the range of altitudes modeled by WACCM3 occur in the lower thermosphere region, where compositional changes can exceed 100% and temperatures increase by over 100 K at solar maximum relative to solar minimum.

[59] 2. Changes in water vapor and temperature at the cold point of the summer mesosphere are 1–2%, and may affect PMC formation.

[60] 3. The solar cycle signal in ozone has a peak in the tropical stratosphere around 40 km and can be in excess of 3%. At the same altitude temperature at the equator are almost 1 K warmer during solar maximum. The tropical ozone column response (~3 DU/100 units of 10.7 cm flux) is less than observed by TOMS and SBUV, but comparable to ground-based estimates.

[61] 4. Indirect effects on ozone via transport of thermospheric NO are apparent in the polar middle and upper stratosphere. In the lower thermosphere, large changes in NO and atomic oxygen can dramatically effect the energy budget, and change how heat is transported to lower atmospheric regions by diffusion.

[62] 5. A small, but statistically significant solar cycle response is seen in tropospheric winds and temperatures.

The signal has similar structure to the observed response but its magnitude is considerably smaller than that observed. This reduction may be caused by fixing SSTs at the lower boundary of the model.

[63] The response of the MLT region in WACCM3 is broadly similar to that of the HAMMONIA model shown in *Schmidt et al.* [2006]. Significant differences in the response of NO exist, but WACCM3 includes a more complete description of auroral and ionospheric processes. If the modeled response of NO is correct, then the solar cycle should have an impact on the ability to detect lower-thermospheric temperature trends due to changes in cooling resulting from anthropogenic increases in CO_2. Since the global mean atmosphere is in approximate thermal balance, differences in heating and cooling rates are balanced by dynamical processes. In the lower thermosphere, the most important of these is thermal diffusion. Heat diffuses downward to a region of the atmosphere where CO_2 cooling is efficient. During solar maximum, the large increase in NO cooling is such that the altitude range over which diffusion cools the upper levels is reduced. Therefore the lower thermospheric temperature response to increasing CO_2 concentrations is larger at solar minimum than solar maximum. The effects of this differing sensitivity to CO_2 trends higher in the atmosphere has been studied by *Qian et al.* [2006].

[64] While this model does include the relatively constant particle precipitation in auroral regions, it does not include all classes of particle inputs. The role of sporadic particle precipitation during solar proton events will be the topic of a separate study using transient simulations with WACCM3. Ionization from galactic cosmic rays and electrons with energies large enough to penetrate into the mesosphere and stratosphere are not included in the current version of WACCM3 either. Finally, the role of the equatorial QBO has not been addressed in this paper because of the fact that WACCM3 does not spontaneously generate a QBO. However, a set of simulations similar to those shown here have been carried out with an externally forced QBO. The effect of the QBO on the solar response, as well as the transfer of the solar signal between atmospheric regions in this model will be addressed in a future study.

References

Austin, J., L. L. Hood, and B. E. Soukharev (2007), Solar cycle variations of stratospheric ozone and temperature in simulations of a coupled chemistry-climate model, *Atmos. Chem. Phys.*, 7, 1693–1706.

Barth, C. A., K. D. Mankoff, S. M. Bailey, and S. C. Solomon (2003), Global observations of nitric oxide in the thermosphere, *J. Geophys. Res.*, 108(A1), 1027, doi:10.1029/2002JA009458.

Beig, G. (2000), The relative importance of solar activity and anthropogenic influences on the ion composition, temperature, and associated neutrals of the middle atmosphere, *J. Geophys. Res.*, 105(D15), 19,841–19,856.

Brasseur, G. P., and S. Solomon (2005), *Aeronomy of the Middle Atmosphere*, 3rd ed., 646 pp., Springer, Dordrecht, Netherlands.

Chandra, S., C. H. Jackman, E. L. Fleming, and J. M. Russell III (1997), The seasonal and long term changes in mesospheric water vapor, *Geophys. Res. Lett.*, 24, 639–642.

Collins, W. D. (1998), A global signature of enhanced shortwave absorption by clouds, *J. Geophys. Res.*, 103(D24), 31,669–31,680.

Collins, W. D., et al (2004), Description of the NCAR Community Atmosphere Model (CAM3), Natl. Cent. For Atmos. Res., Boulder, Colo.

Coughlin, K., and K. K. Tung (2004), Eleven-year solar cycle signal throughout the lower atmosphere, *J. Geophys. Res.*, 109, D21105, doi:10.1029/2004JD004873.

Crooks, S. A., and L. J. Gray (2005), Characterization of the 11-year solar cycle signal using a multiple regression analysis of the ERA-40 dataset, *J. Clim.*, 18, 996–1015.

DeLand, M. T., E. P. Shettle, G. E. Thomas, and J. J. Olivero (2003), Solar backscattered ultraviolet (SBUV) observations of polar mesospheric clouds (PMCs) over two solar cycles, *J. Geophys. Res.*, 108(D8), 8445, doi:10.1029/2002JD002398.

DeLand, M. T., E. T. Shettle, G. E. Thomas, and J. J. Olivero (2006), A quarter-century of satellite polar mesospheric cloud observations, *J. Atmos. Sol. Terr. Phys.*, 68(1), 9–29.

Dunkerton, T., D. Delisi, and M. Baldwin (1998), Middle atmosphere cooling trend in historical rocketsonde data, *Geophys. Res. Lett.*, 25, 3371–3374.

Egorova, T., E. Rozanov, E. Manzini, M. Haberreiter, W. Schmutz, V. Zubov, and T. Peter (2004), Chemical and dynamical response to the 11-year variability of the solar irradiance simulated with a chemistry-climate model, *Geophys. Res. Lett.*, 31, L06119, doi:10.1029/2003GL019294.

Eyring, V., et al. (2006), Assessment of temperature, trace species, and ozone in chemistry-climate model simulations of the recent past, *J. Geophys. Res.*, 111, D22308, doi:10.1029/2006JD007327.

Fomichev, V. I., J. P. Blanchet, and D. S. Turner (1998), Matrix parameterization of the 15 μm CO_2 band cooling in the middle and upper atmosphere for variable CO_2 concentration, *J. Geophys. Res.*, 103, 11,505–11,528.

Fomichev, V. I., V. P. Ogibalov, and S. R. Beagley (2004), Solar heating by the near-IR CO_2 bands in the mesosphere, *Geophys. Res. Lett.*, 31, L21102, doi:10.1029/2004GL020324.

Froehlich, C. (2000), Observations of Irradiance Variations, *Space Sci. Rev.*, 94, 15–24.

Froidevaux, L., M. Allen, S. Berman, and A. Daughton (1989), The mean ozone profile and its temperature sensitivity in the upper stratosphere and lower mesosphere: an analysis of LIMS observations, *J. Geophys. Res.*, 94, 6389–6417.

Garcia, R. R., S. Solomon, R. G. Roble, and D. W. Rusch (1984), A numerical response of the middle atmosphere to the 11-year solar cycle, *Planet. Space Sci.*, 32, 411–423.

Garcia, R. R., D. R. Marsh, D. E. Kinnison, B. A. Boville, and F. Sassi (2007), Simulations of secular trends in the middle atmosphere, 1950–2003, *J. Geophys. Res.*, 112, D09301, doi:10.1029/2006JD007485.

Haigh, J. D. (1994), The role of stratospheric ozone in modulating the solar radiative forcing of climate, *Nature*, 370, 544–546.

Haigh, J. D. (1999), The impact of solar variability on climate, *Science*, 272, 981–984.

Haigh, J. D. (2003), The effects of solar variability on the Earths climate, *Philos. Trans. R. Soc. London, Ser. A*, 362, 95–111.

Haigh, J. D., M. Blackburn, and R. Day (2005), The response of tropospheric circulation to perturbations in the lower-stratopshere, *J. Clim.*, 18, 3672–3685.

Hervig, M., and D. Siskind (2006), Decadal and inter-hemispheric variability in polar mesospheric clouds, water vapor, and temperature, *J. Atmos. Sol. Terr. Phys.*, 68, 30–41.

Hood, L. L. (2004), Effects of solar UV variability on the stratosphere, in *Solar Variability and its Effects on Climate, Geophys. Monogr. Ser.*, vol. 141, edited by J. M. Pap and P. Fox, pp. 283–303, AGU, Washington, D. C.

Hood, L. L., and B. E. Soukharev (2006), Solar induced variations of odd nitrogen: Multiple regression analysis of UARS HALOE data, *Geophys. Res. Lett.*, 33, L22805, doi:10.1029/2006GL028122.

Hurrell, J. W., J. J. Hack, A. S. Phillips, J. Caron, and J. Yin (2006), The dynamical simulation of the Community Atmosphere Model Version 3 (CAM3), *J. Clim.*, 19, 2162–2183.

Jackman, C. H., M. T. DeLand, G. J. Labow, E. L. Fleming, D. K. Weisenstein, M. K. W. Ko, M. Sinnhuber, J. Anderson, and J. M. Russell (2005), The influence of the several very large solar proton events in years 2000–2003 on the neutral atmosphere, *Adv. Space Res.*, 35(3), 445–450.

Kaufmann, M., O. A. Gusev, K. U. Grossmann, F. J. Martin-Torres, D. R. Marsh, and A. A. Kutepov (2003), Satellite observations of day- and nighttime ozone in the mesosphere and lower thermosphere, *J. Geophys. Res.*, 108(D9), 4272, doi:10.1029/2002JD002800.

Keating, G. M., M. C. Pitts, G. Brasseur, and A. DeRudder (1987), Response of middle atmosphere to short-term solar ultraviolet variations: 1. Observations, *J. Geophys. Res.*, 92, 889–902.

Kinnison, D. E., et al. (2007), Sensitivity of chemical tracers to meteorological parameters in the MOZART3 chemical transport model, *J. Geophys. Res.*, *112*, D20302, doi:10.1029/2006JD007879.

Kockarts, G. (1980), Nitric oxide cooling in the terrestrial thermosphere, *Geophys. Res. Lett.*, *7*, 137–140.

Kodera, K., and Y. Kuroda (2002), Dynamical response to the solar cycle, *J. Geophys. Res.*, *107*(D24), 4749, doi:10.1029/2002JD002224.

Koppers, G. A. A., and D. P. Murtagh (1996), Model studies of the influence of O_2 photodissociation parameterizations in the Schumann-Runge bands on ozone related photolysis in the upper atmosphere, *Ann. Geophys.*, *14*, 68–79.

Labitzke, K., J. Austin, N. Butchart, J. Knight, M. Takahashi, M. Nakamoto, T. Nagashima, J. Haigh, and V. Williams (2002), The global signal of the 11-year solar cycle in the stratosphere: Observations and models, *J. Atmos. Sol. Terr. Phys.*, *64*(2), 203–210.

Langematz, U., J. L. Grenfell, K. Matthes, P. Mieth, M. Kunze, B. Steil, and C. Brühl (2005), Chemical effects in 11-year solar cycle simulations with the Freie Universitat Berlin Climate Middle Atmosphere Model with online chemistry (FUBCMAM- CHEM), *Geophys. Res. Lett.*, *32*, L13803, doi:10.1029/2005GL022686.

Lean, L., J. Rottman, G. J. Kyle, H. L. Woods, T. N. Hickey, and J. R. Pugga (1997), Detection and parameterization of variations in solar mid and-near-ultraviolet radiation (200–400 nm), *J. Geophys. Res.*, *102*, 29,939–29,956.

Lee, H., and A. K. Smith (2003), Simulations of the combined effects of solar cycle, quasi-biennial oscillation, and volcanic forcing on stratospheric ozone changes in recent decades, *J. Geophys. Res.*, *108*(D2), 4049, doi:10.1029/2001JD001503.

Lin, S.-J. (2004), A vertically Lagrangian finite-volume dynamical core for global models, *Mon. Weather Rev.*, *132*, 2293–2307.

Madronich, S. (1989), Photodissociation in the atmosphere: 1. Actinic flux and effect of ground reflection and clouds, *J. Geophys. Res.*, *92*, 9740–9752.

Maeda, S., T. J. Fuller-Rowell, and D. S. Evans (1989), Zonally averaged dynamical and compositional response of the thermosphere to auroral activity during September 18–24, 1984, *J. Geophys. Res.*, *94*, 16,869–16,883.

Marsh, D. R., W. R. Skinner, A. R. Marshall, P. B. Hays, D. A. Ortland, and J.-H. Yee (2002), High Resolution Doppler Imager observations of ozone in the mesosphere and lower thermosphere, *J. Geophys. Res.*, *107*(D19), 4390, doi:10.1029/2001JD001505.

Marsh, D. R., S. C. Solomon, and A. E. Reynolds (2004), Empirical model of nitric oxide in the lower thermosphere, *J. Geophys. Res.*, *109*, A07301, doi:10.1029/2003JA010199.

Matthes, K., K. Kodera, J. D. Haigh, D. T. Shindell, K. Shibata, U. Langematz, E. Rozanov, and Y. Kuroda (2003), GRIPS Solar Experiments Intercomparison Project: Initial results, *Pap. Meteorol. Geophys.*, *54*(2), 71–90.

McCormack, J. P., and L. L. Hood (1996), Apparent solar cycle variations of upper stratosphere ozone and temperature: Latitude and seasonal dependences, *J. Geophys. Res.*, *101*, 20,933–20,994.

Minschwaner, K., and D. E. Siskind (1993), A new calculation of nitric oxide photolysis in the stratosphere, mesosphere, and lower thermosphere, *J. Geophys. Res.*, *98*, 20,401–20,412.

Mlynczak, M. G., and S. Solomon (1993), A detailed evaluation of the heating efficiency in the middle atmosphere, *J. Geophys. Res.*, *98*(D6), 10,517–10,541.

Mlynczak, M. G., C. J. Mertens, R. R. Garcia, and R. W. Portmann (1999), A detailed evaluation of the stratospheric heat budget 2. Global radiation balance and diabatic circulations, *J. Geophys. Res.*, *104*, 6039–6066.

Ogibalov, V. P., and V. I. Fomichev (2003), Parameterization of solar heating by the near IR CO_2 bands in the mesosphere, *Adv. Space Res.*, *32*, 759–764.

Picone, J. M., A. E. Hedin, D. P. Drob, and A. C. Aikin (2002), NRLMSISE-00 empirical model of the atmosphere: Statistical comparisons and scientific issues, *J. Geophys. Res.*, *107*(A12), 1468, doi:10.1029/2002JA009430.

Qian, L., R. G. Roble, S. C. Solomon, and T. J. Kane (2006), Calculated and observed climate change in the thermosphere, and a prediction for solar cycle 24, *Geophys. Res. Lett.*, *33*, L23705, doi:10.1029/2006GL027185.

Ramaswamy, V., et al. (2001), Stratospheric temperature trends: Observations and model simulations, *Rev. Geophys.*, *39*(1), 71–122.

Randall, C. E., D. W. Rusch, R. M. Bevilacqua, K. W. Hoppel, and J. D. Lumpe (1998), Polar ozone and aerosol meausurement (POAM) II stratospheric NO_2, 1993–1996, *J. Geophys. Res.*, *103*(D21), 28,361–28,371.

Randall, C. E., D. E. Siskind, and R. M. Bevilacqua (2001), Stratospheric NO_x Enhancements in the Southern Hemisphere vortex in winter/spring of 2000, *Geophys. Res. Lett.*, *28*(12), 2385–2388.

Randel, W. J., and F. Wu (2007), A stratospheric ozone profile data set for 1979–2005: Variability, trends, and comparisons with column ozone data, *J. Geophys. Res.*, *112*, D06313, doi:10.1029/2006JD007339.

Remsberg, E. E., and L. E. Deaver (2005), Interannual, solar cycle, and trend terms in middle atmospheric temperature time series from HALOE, *J. Geophys. Res.*, *110*, D06106, doi:10.1029/2004JD004905.

Rind, D., J. Perlwitz, and P. Lonergan (2005), AO/NAO response to climate change: 1. Respective influences of stratospheric and tropospheric climate changes, *J. Geophys. Res.*, *110*, D12107, doi:10.1029/2004JD005103.

Roble, R. G. (1995), Energetics of the mesosphere and thermosphere, in *The Upper Mesosphere and Lower Thermosphere: A Review of Experiment and Theory*, *Geophys. Monogr. Ser.*, vol. 87, edited by R. M. Johnson and T. L. Killeen, pp. 1–21, AGU, Washington, D. C.

Roble, R. G., and E. C. Ridley (1994), A thermosphere-ionosphere-mesosphere-electrodynamics general circulation model (TIME-GCM): Equinox solar cycle minimum simulations (30–500 km), *Geophys. Res., Lett.*, *21*, 417–420.

Roble, R. G., R. E. Dickinson, and E. C. Ridley (1982), Global circulation and temperature structure of thermosphere with high-latitude plasma convection, *J. Geophys. Res.*, *87*, 1599–1614.

Roble, R. G., E. C. Ridley, and R. E. Dickinson (1987), On the global mean structure of the thermosphere, *J. Geophys. Res.*, *92*, 8745–8758.

Rozanov, E. V., M. E. Schlesinger, T. A. Egorova, B. Li, N. Andronova, and V. A. Zubov (2004), Atmospheric response to the observed increase of solar UV radiation from solar minimum to solar maximum simulated by the University of Illinois at Urbana-Champaign climate-chemistry model, *J. Geophys. Res.*, *109*, D01110, doi:10.1029/2003JD003796.

Rozanov, E., L. Callis, M. Schlesinger, F. Yang, N. Andronova, and V. Zubov (2005), Atmospheric response to NOy source due to energetic electron precipitation, *Geophys. Res. Lett.*, *32*, L14811, doi:10.1029/2005GL023041.

Russell, J. M., III, M. G. Mlynczak, L. L. Gordley, J. Tansock, and R. Esplin (1999), An overview of the SABER experiment and preliminary calibration results, *Proc. SPIE Int. Soc. Opt. Eng.*, *3756*, 277–288, doi:10.1117/12.366382.

Sander, S. P., et al (2003), Chemical kinetics and photochemical data for use in atmospheric studies, evaluation 14, *JPL Publ. 02-25*, NASA Jet Propul. Lab., Pasadena, Calif.

Sassi, F., R. R. Garcia, B. A. Boville, and H. Liu (2002), On temperature inversions and the mesospheric surf zone, *J. Geophys. Res.*, *107*(D19), 4380, doi:10.1029/2001JD001525.

Scaife, A. A., J. Austin, N. Butchart, S. Pawson, M. Keil, J. Nash, and I. N. James (2000), Seasonal and interannual variability of the stratosphere diagnosed from UKMO TOVS analyses, *Q. J. R. Meteorol. Soc.*, *126*, 2585–2604.

Schmidt, H., G. Brasseur, M. Charron, E. Manzini, M. A. Giorgetta, V. Fomichev, D. Kinnison, D. Marsh, and S. Walters (2006), The HAMMONIA Chemistry Climate Model: Sensitivity of the mesopause region to the 11-year solar cycle and CO_2 doubling, *J. Clim.*, *19*, 3903–3931, doi:10.1175/JCLI3829.1.

Shindell, D., D. Rind, N. Balachandran, J. Lean, and J. Lonergan (1999), Solar cycle variability, ozone, and climate, *Science*, *284*, 305–308.

Shindell, D. T., G. Faluvegi, and N. Bell (2003), Preindustrial-to-present-day radiative forcing by tropospheric ozone from improved simulations with the GISS chemistry-climate GCM, *Atmos. Chem. Phys.*, *3*, 1675–1702.

Siskind, D. E. (2000), On the coupling between middle and upper atmospheric odd nitrogen, in *Atmospheric Science Across the Stratopause*, *Geophys. Monogr. Ser.*, vol. 123, edited by D. E. Siskind, S. D. Eckermann, and M. E. Summers, pp. 101–116, AGU, Washington, D. C.

Solomon, S. C., and L. Qian (2005), Solar extreme-ultraviolet irradiance for general circulation models, *J. Geophys. Res.*, *110*, A10306, doi:10.1029/2005JA011160.

Soukharev, B. E., and L. L. Hood (2006), Solar cycle variation of stratospheric ozone: Multiple regression analysis of longterm satellite data sets and comparisons with models, *J. Geophys. Res.*, *111*, D20314, doi:10.1029/2006JD007107.

Thejll, P., B. Christiansen, and H. Gleisner (2003), On correlations between the North Atlantic Oscillation, geopotential heights, and geomagnetic activity, *Geophys. Res. Lett.*, *30*(6), 1347, doi:10.1029/2002GL016598.

Tourpali, K., C. Schuurmans, R. van Dorland, B. Steil, and C. Brühl (2003), Stratospheric and tropospheric response to enhanced solar UV radiation: A model study, *Geophys. Res. Lett.*, *30*(5), 1231, doi:10.1029/2002GL016650.

van Loon, H., and K. Labitzke (2000), The influence of the 11-year solar cycle on the stratosphere below 30 km: A review, *Space Sci. Rev.*, *94*, 259–278.

Woods, T., and G. Rottman (2002), Solar ultraviolet variability over time periods of aeronomic interest, in *Atmospheres in the Solar System:*

Comparative Aeronomy, Geophys. Monogr. Ser., vol. 130, edited by M. Mendillo, A. Nagy, and J. H. Waite Jr., pp. 221–234, AGU, Washington, D. C.

Woods, T. N., W. K. Tobiska, G. J. Rottman, and J. R. Worden (2000), Improved solar Lyman α irradiance modeling from 1947 through 1999 based on UARS observations, *J. Geophys. Res.*, *105*, 27,195–27,215.

World Meteorological Organization (2003), Scientific assessment of ozone depletion: 2002, *Global Res. and Monit. Proj. Rep.*, *47*, 498 pp., Geneva, Switzerland.

————————————

B. A. Boville, R. R. Garcia, D. E. Kinnison, D. R. Marsh, F. Sassi, and S. C. Solomon, Atmospheric Chemistry Division, National Center for Atmospheric Research, P.O. Box 3000, Boulder, CO 80307-3000, USA. (marsh@ucar.edu)

K. Matthes, Institut für Meteorologie, Freie Universität Berlin, D-12165 Berlin, Germany.